Key Points:

- Slab breakoff leads to coeval uplift of the foreland basin and adjacent mountain range, with the latter leading to enhanced sediment supply
- Third-order eustatic cycles do not mask the tectonostratigraphic signal from slab breakoff in a foreland basin
- The Early Miocene stratigraphic record of the Austrian Molasse may have been controlled by European slab breakoff

The Tectonostratigraphic Expression of Slab Breakoff in Foreland Basins: Insights From 2D Forward Stratigraphic Modeling

L. H. J. Eskens[1] ⓘ, A. Piccolo[2,3] ⓘ, M. Thielmann[2,4] ⓘ, B. Claussmann[5], M. Lejri[6], T. A. Ehlers[7] ⓘ, and N. Andrić-Tomašević[1] ⓘ

[1]Karlsruhe Institute of Technology, Institute of Applied Geosciences, Karlsruhe, Germany, [2]Bayerisches Geoinstitut, University of Bayreuth, Bayreuth, Germany, [3]School of Earth and Environment, University of Leeds, Leeds, UK, [4]Institute of Geosciences, University of Bonn, Bonn, Germany, [5]SLB UK, SLB Abingdon Technology Centre, Abingdon, UK, [6]SLB Norway, SLB Norway Technology Center, Oslo, Norway, [7]School of Geographical and Earth Sciences, University of Glasgow, Glasgow, UK

Abstract Changes in foreland basin architecture have been attributed to slab breakoff based on qualitative assessments of geological data. However, this cause-effect relationship has not been evaluated quantitatively. In this contribution, we use a one-way coupling approach between 2D thermomechanical models of slab breakoff and 2D stratigraphic forward models of a pro-foreland basin. This allows a quantitative investigation of the first order tectonostratigraphic signal from slab breakoff in a foreland basin while isolating it from other processes controlling the basin evolution. We investigate the effects of slab breakoff on foreland basin evolution by varying the (a) initial subduction angle and (b) mantle viscosity. Furthermore, we assess whether eustacy can mask the stratigraphic signal from slab breakoff by introducing third-order eustatic cycles. Results highlight that both the final phase of slab necking and subsequent breakoff generally yield higher uplift rates of both the foreland basin (between 0.09 and 25 km/Myr) and mountain range (between 0.13 and 30 km/Myr) for successively steeper slabs and decreased mantle viscosity. In turn, breakoff causes a pulse in sediment supply to the foreland (up to 2.6E10 m³/Myr) due to mountain range uplift. In the models, eustacy has no significant effect on preserving the stratigraphic signal from slab breakoff and the induced underfill to overfill transition. Increasing mantle viscosity promotes a prolonged necking phase that imposes a long-lasting, but weak uplift and related increase in sediment supply. Lastly, first-order features induced by slab breakoff observed on synthetic seismic profiles of our models bear resemblance to reflection seismic data from the Austrian Molasse Basin, where slab breakoff has been suggested to have influenced the basin evolution.

1. Introduction

Peripheral pro-foreland basins (from here on referred to as foreland basins) develop adjacent to growing mountain ranges due to topographic- and slab loading causing flexural bending of the downgoing foreland plate (Beaumont, 1981; Catuneanu, 2004; DeCelles, 2012; DeCelles & Giles, 1996; Flemings & Jordan, 1989; Jordan, 1981; Naylor & Sinclair, 2008). The sedimentary fill records the basin evolution in both time and space resulting from the interplay between tectonic, climatic, and eustatic forcings (Flemings & Jordan, 1990; Jordan & Flemings, 1991; Sinclair et al., 1991; Van der Meulen et al., 1998).

A major architectural change observed in many foreland basins (e.g., Northern Alpine Foreland Basin (NAFB), Taiwan, Apenninnic and Alborz foreland basins; Covey, 1986; Kuhlemann & Kempf, 2002; Meulenkamp et al., 1996; Wilmsen et al., 2009) is the transition from under- to overfilled deposition. Underfilled deposition implies that the rate of accommodation space generation outpaces sediment supply leading to either aggrading or retrograding stacking patterns. In contrast, overfilled deposition indicates the opposite, and is characterized by prograding stacking patterns (Catuneanu et al., 2011). During this transition, pelagic deposition indicating sediment starvation will grade stratigraphically upward into non-condensed, coarse-grained marine, shelf-, littoral, and/or lacustrine sedimentation. Thus, this transition represents a rapid decrease in relative water level.

As foreland basin development is strongly coupled to that of the adjacent mountain range and its climatic history (e.g., DeCelles, 2012), this change in depositional style hints at changes in the process(es) that control the generation of accommodation space and/or sediment supply. Increases in sediment supply from the adjacent orogenic wedge (NAFB, Hülscher et al., 2019; Kuhlemann & Kempf, 2002), slab tearing- and breakoff (NAFB,

Software: L. H. J. Eskens, A. Piccolo
Supervision: B. Claussmann, M. Lejri, N. Andrić-Tomašević
Validation: B. Claussmann, M. Lejri
Visualization: L. H. J. Eskens, A. Piccolo
Writing – original draft: L. H. J. Eskens
Writing – review & editing: A. Piccolo, M. Thielmann, B. Claussmann, M. Lejri, T. A. Ehlers, N. Andrić-Tomašević

Alborz, and Appenninic foreland basins, Ascione et al., 2012; Meulenkamp et al., 1996; Schlunegger & Castelltort, 2016; Schlunegger & Kissling, 2022; Sinclair, 1997; Sinclair & Allen, 1992; Van der Meulen et al., 1998; Wilmsen et al., 2009), and/or eustacy (NAFB, Diem, 1986; Flemings & Jordan, 1990, numerical studies; Jordan & Flemings, 1991; Lemcke, 1988) have been suggested to control foreland basin architecture, and potentially to drive the transition from sediment starvation to non-condensed prograding deposition. In this contribution, we investigate whether slab breakoff can indeed induce the onset of progradation of overfilled (i.e., non-condensed) deposition, and aim to define its tectonostratigraphic fingerprint preserved in the basin fill more robustly.

Slab breakoff (also called slab detachment) is the process during which the lower part of a subducting slab separates from its upper segment and subsequently sinks into the mantle (Isacks & Molnar, 1969; Wortel & Spakman, 2000). Previous geodynamic studies have shown that the predominant deformation mechanism during slab breakoff is viscous thinning of the subducting plate (e.g., Baumann et al., 2010; Burov & Yamato, 2008; Duretz et al., 2012). This process occurs at greater depths and requires more time for older slabs, increased convergence rates, and/or mantle viscosity (e.g., Baumann et al., 2010; Duretz et al., 2011; Gerya et al., 2004; van Hunen and Allen, 2011). The resultant loss of the vertical slab pull induces an isostatically-driven uplift of both the mountain range (with rates of up to 19.4 km/Myr, Buiter et al., 2002; Duretz et al., 2011; Gerya et al., 2004) and the adjacent foreland basin (with rates between 0.1 and 2.65 km/Myr, Andrews & Billen, 2009; Duretz et al., 2011).

Slab breakoff causes isostatic rebound of the foreland plate, resulting in the uplift of the basin floor of the foreland basin and adjacent mountain range (Duretz et al., 2011; Gerya et al., 2004; van Hunen and Allen, 2011). If the foreland basin is connected to the global oceans, the uplift of the basin floor will result in a decrease in the relative sea level. Additionally, increased topographic slope steepness and a high frequency of earthquakes related to slab breakoff (e.g., in the present-day Hindu-Kush or the Vrancea region in Romania, Kufner et al., 2017, 2021; Sperner et al., 2001) increase the frequency of slope collapse events. Additionally, increases in orographic precipitation on uplifted windward slopes of the mountain range will favor higher erosion rates (Ehlers & Poulsen, 2009). The combination of these effects will result in increased sediment supply toward the adjacent foreland basin (Croissant et al., 2019; Montgomery & Brandon, 2002; Ouchi, 2011). Subsequently these processes induced by slab breakoff may force a transition from underfilled to overfilled conditions in the foreland basin (Garefalakis & Schlunegger, 2018; Handy, 2025; Koshnaw et al., 2024; Sinclair, 1997).

This study investigates the stratigraphic signal from slab breakoff in a foreland basin. To this end, we utilize a one-way coupling between 2D geodynamic models (GMs) simulating slab breakoff with 2D stratigraphic forward models (SFMs) for an orogen-foreland system. This allows us to isolate the tectonostratigraphic signal related to slab breakoff from other external and/or intrinsic processes that leave fingerprints in a foreland basin's stratigraphic fill. We test the effects of different slab breakoff scenarios by varying the (a) initial subduction angle and (b) mantle viscosity in the GMs. These parameters are chosen as they control the time-transgressive changes in slab pull, and, thereby, the isostatic response at the surface. The potential impact of third-order eustatic cycles (50 m amplitude, 1 My period) is also tested to investigate whether sea level variations can mask the stratigraphic signal from slab breakoff. Although our models are not aimed at reproducing a particular foreland basin, we compare our results with the Austrian Molasse Basin (eastern part of the NAFB) to discuss the potential preservation of the tectonostratigraphic signal of slab breakoff for this natural example.

2. Material and Methods

This contribution aims to quantitatively evaluate the stratigraphic signal induced by slab breakoff in a foreland basin. To this end, we use a one-way coupling approach between GMs simulating slab breakoff constructed in LaMEM (Kaus et al., 2016; Piccolo et al., 2022) with SFMs using the Geological Process Modeling (GPM) software in Petrel from SLB (Tetzlaff & Harbaugh, 1989). In the following subsections, we introduce the LaMEM (Section 2.1) and GPM (Section 2.2) models. Subsequently, we outline the general modeling workflow employed during this study (Section 2.3). Lastly, we give a description of the setups used to simulate different slab breakoff scenarios in LaMEM (Section 2.4.1) of which the output is used to constrain the tectonics in the corresponding SFMs in the GPM software (Section 2.4.2).

To isolate the effect of slab necking- and breakoff on (vertical) tectonics, the GMs focus solely on slab breakoff. Therefore, our GMs do not include plate convergence. Furthermore, to quantify uplift and subsidence rates purely induced by slab breakoff, the GMs do include surface processes which could modify the signal. Surface processes
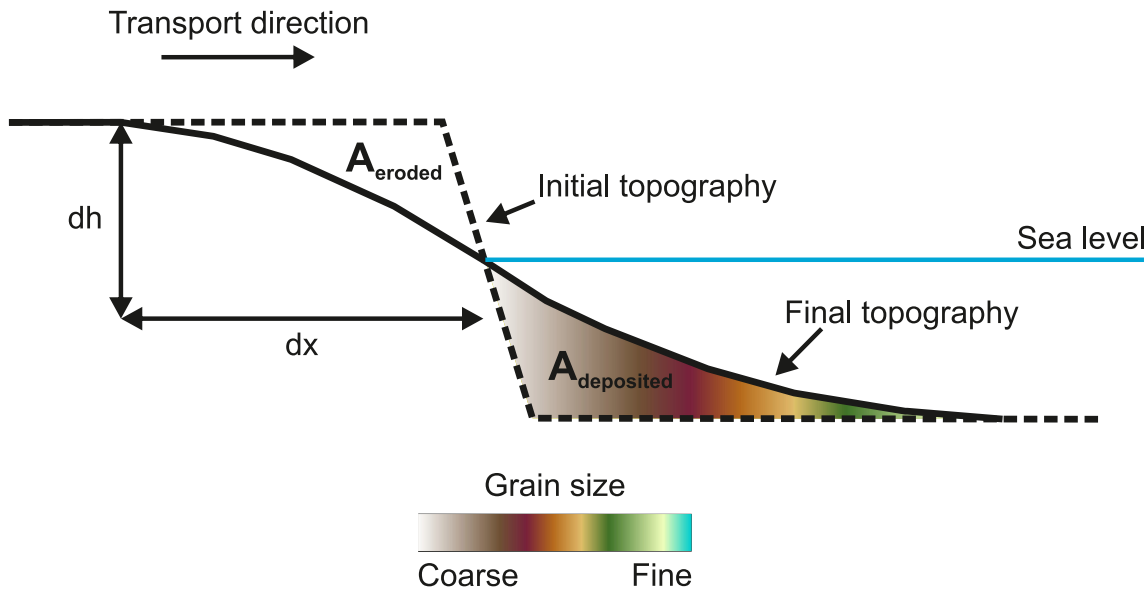
Figure 1. Schematic representation of diffusion in Geological Process Modeling of multiple sediment types. A_{eroded} is the area of the initial topography that is eroded after time increment dt and is equal to the area $A_{deposited}$ downslope.

are considered in the SFMs. Through this approach, our one-way coupling approach allows us to narrow down the first-order tectonostratigraphic response from slab breakoff in a foreland basin and to clearly differentiate its effects from surface processes or sea-level variations. However, the instantaneous values for uplift and subsidence presented in this work do not represent average values derived from the geological record. Despite this, the workflow allows us to discern first-order trends in terms of changes in basin response to geodynamic forcings.

2.1. LaMEM

LaMEM is a staggered finite difference code, solving a coupled system of the momentum, mass (Stokes equations), and energy conservation equations. These equations are solved in a Cartesian grid employing the *Boussinesq* approximation (Boussinesq, 1897; Kaus et al., 2016; Piccolo et al., 2022). The material properties for each lithotype are advected using markers that additionally carry historical values such as temperature, total plastic deformation, and stress tensor components. The markers are advected after each timestep, and the stored information is interpolated into the computational grid. For an in-depth description of the equations solved in LaMEM, we invite the reader to Text S1 in Supporting Information S1.

2.2. Geological Process Modeling

The GPM software, developed by SLB, is a simulator for stratigraphic and sedimentary processes (Tetzlaff & Harbaugh, 1989) and is integrated into the Petrel E&P software platform. GPM allows for modeling of the erosion, transport, and deposition of clastic sediments and the in situ growth of carbonates (independently or concurrently) in different geological settings. This can be done in either 2D or 3D. The erosion, transport, and deposition can be simulated either as solely being diffusional or, additionally, flow-driven (i.e., advection). We assume sediment erosion, transport, and deposition on an orogen-foreland basin scale to be driven exclusively by diffusion, in line with similar studies (Flemings & Jordan, 1990; Jordan & Flemings, 1991; Sinclair et al., 1991).

Sediment diffusion is the dispersion of erosional material on the topographic slope driven by gravity, meaning that a steep slope will smoothen over time (Figure 1). The resulting redistribution of mass and change in topography can be described with Equation 1;

$$\frac{\partial h}{\partial t} = D \frac{\partial^2 h}{\partial x^2}$$

(1)

Table 1
Depositional Facies Classification in the Forward Stratigraphic Models Based on the Simulation Results

Facies				
Conditions	Littoral and neritic	Slope/shelf	Basin axis	Coarse-grained deep-water turbidites
D (depositional water depth) [m]	<100	$100 < D < 500$	>500	>500
Coarse sand content [%]	>40	>45	<5	>40
Fine sand content [%]	>20	>20	<50	>20
Silt content [%]	<20	<20	>5	<20
Clay content [%]	<20	<15	>5	<20

Note. Any combination of depositional water depths and sediment type distributions not covered by the listed conditions is labeled as "marine." Water depths are based on Allen (1965), Okosun and Osterloff (2014).

Here, h is the topographic variation in a cell in the model in m, t the time increment between different model increments in yr, x the width of a cell in m, and D the diffusivity in m^2/yr.

In GPM, the integration of variations in transportability and erodibility of different rock types/sediments, as well as the dependency of diffusion on topography (i.e., climate and higher average slope steepness at higher elevation), can be included in the modeling. This is achieved by calculating D, obtained through multiplying a prescribed D_c (with a unit of m^2/yr) with unitless coefficients representing these dependencies. As such, the diffusion rate in m^2/yr is calculated using Equation 2 in case the basement is being eroded;

$$D = D_c * T_S * C(z) * E_b \tag{2}$$

In case the formerly deposited sediments are eroded, Equation 2 becomes Equation 3;

$$D = D_c * T_S * C(z) * E_s \tag{3}$$

D_c is a prescribed diffusion coefficient and is a unitless multiplier. T_s is the transportability factor, which depends on sediment type, and is also a unitless multiplier. Lower values are assigned to fine sediment to enable greater transport distances than coarse sediment under similar topographic conditions. This allows for grain size differentiation in the foreland deposits. $C(z)$ is a curve describing the dependency of the diffusivity on the topography *w.r.t.* sea level at each timestep. E_s and E_b are the erodibility coefficients for the sediment type and basement topography, respectively, and are unitless multipliers. A value for E_s is calculated depending on the volumetric contribution of each sediment type in the mixture.

The active layer thickness (ALT) defines the maximum amount of topography that can be eroded during each time step. Furthermore, the elastic compaction of sediments due to overburden is calculated based on the initial porosity and a compaction coefficient of the respective (mix of) sediment type(s). Conceptually, the compaction coefficient reflects the Youngs's modulus, but is applied to long-term compaction due to overburden. Lastly, tectonics in GPM can only be modeled for vertical motion. This means that the effects of horizontal tectonics, like overthrusting, cannot be accounted for. During vertical tectonic movements derived from slab breakoff, the sea level remains stationary, allowing for the modeling of basins that are connected to the global oceans.

2.3. Model Coupling

This contribution utilizes a one-way coupling between the GMs constructed in LaMEM with the SFMs in GPM to quantitatively analyze the first-order tectonostratigraphic development of a foreland basin during slab breakoff. We extract uplift- and subsidence profiles of the free surface in response to slab breakoff for different geodynamic settings in our GMs (Section 2.4.1). These are used as tectonic input in GPM, wherein the changes in surface processes and resulting foreland basin architecture are modeled. The main outputs of the GPM models are maps of sediment thicknesses, which allow for calculating the sediment supply rates to the basin through time. Furthermore, we calculate the volume of tectonic-induced loss/generation of accommodation space. Information from Wheeler diagrams for the (average) grain size distribution and depositional water depth was combined to generate
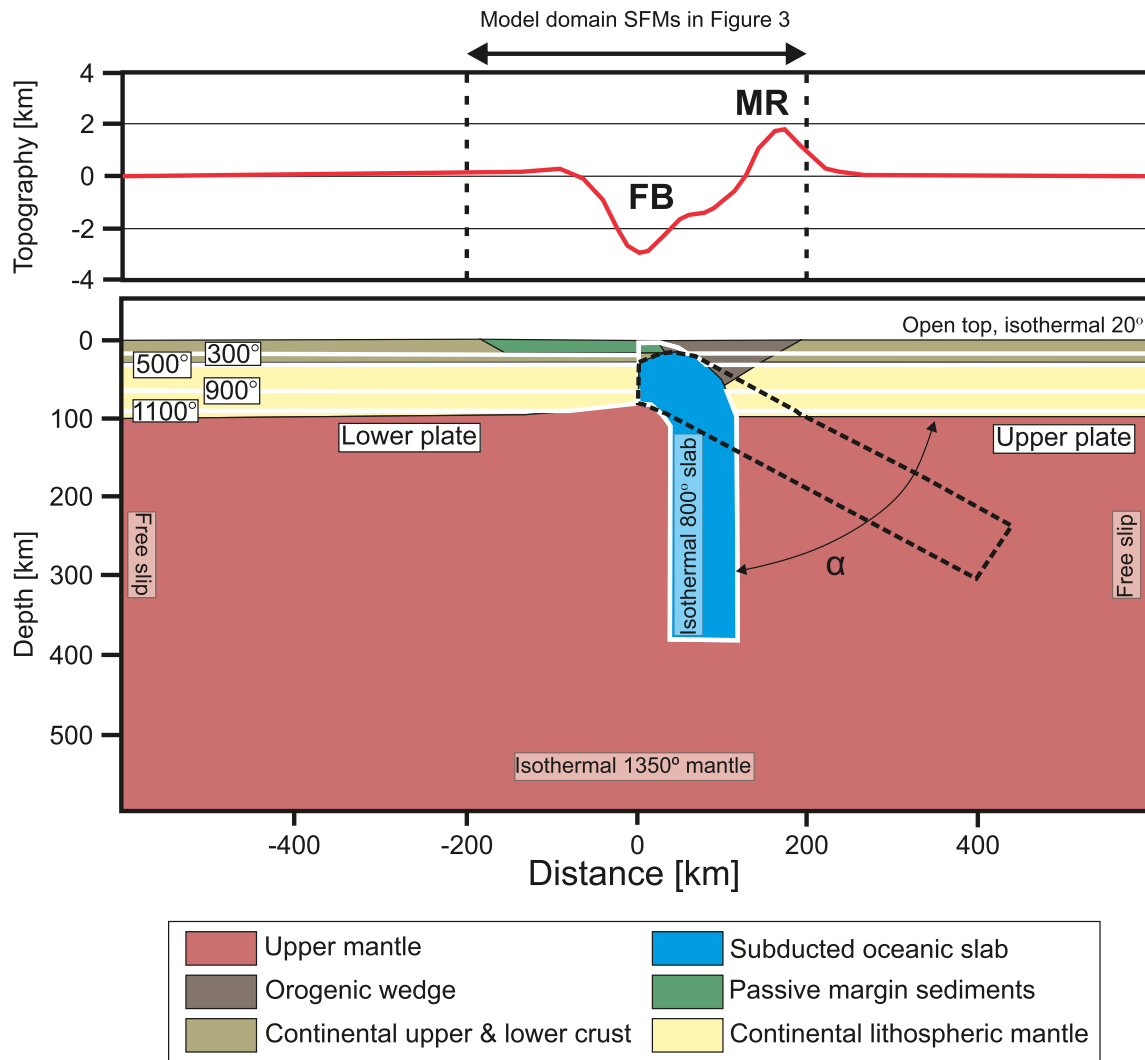
Figure 2. Schematic representation of initial conditions in the geodynamic model used for this study. The upper panel shows the initial surface topography, which is the same at the start of each model run. The model domain of the stratigraphic forward models is highlighted. The lower panel shows the lithospheric structure. There is no flux at the lateral model boundaries. Angle α is 30°, 45°, 60°, or 90°. FB = foreland basin, MR = mountain range.

depositional facies models (Table 1). Lastly, the porosity and pressure distribution were used to construct synthetic seismic profiles (Text S2 in Supporting Information S1).

2.4. Experimental Setups

2.4.1. Geodynamic Models for Different Slab Breakoff Scenarios

The GM setup represents a simplified post-collisional stage of an orogen evolution in which an oceanic slab is still attached to the lower plate (Figure 1). The domain spans from −1,000 to 1,000 km in the horizontal direction and from −1,000 to 50 km in the vertical direction (Figure 1). The numerical grid on which the model is resolved is made of 2,049 and 1,025 nodes in the horizontal- and vertical directions, respectively. There is no post-collisional convergence and, thereby, no tectonic shortening in the orogenic wedge. Therefore, slab necking- and subsequent breakoff are caused by the negative buoyancy force (i.e., slab pull) of an isothermal (800°C) slab in an isothermal (1,350°C) mantle (Figure 2). The 800°C derives from an oceanic slab with an age of 30 Myr based on the halfspace cooling model (Turcotte & Schubert, 2002). We use an isothermal slab because it is easier to have an initial model setup in isostatic balance (Spang et al., 2022). We neglect the adiabatic processes in the mantle, with 1,350°C representing the potential mantle temperature (Afonso et al., 2008 and references therein). The slab has a
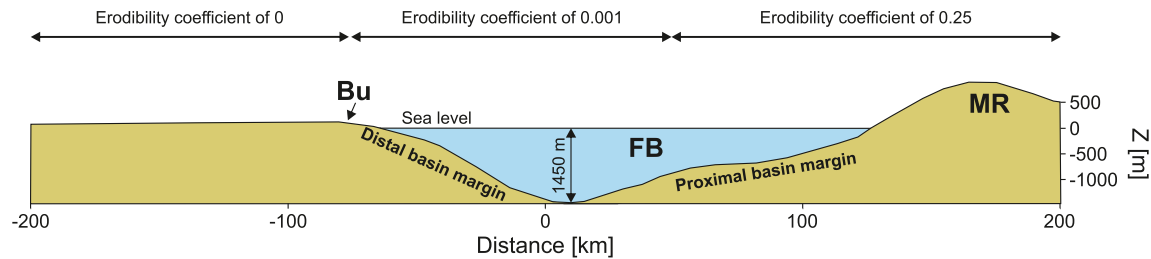
Figure 3. Schematic representation of initial conditions in stratigraphic forward models constructed in this study. The basement consists of 25% coarse sand, fine sand, silt, and clay. FB = foreland basin, MR = mountain range, Bu = forebulge.

thickness of $D_0 = 80$ km (Holt et al., 2017; Schmalholz, 2011) and length of $L_r = 300$ km (Figure 2). We choose to use a small initial slab length to make sure the slab does not reach the 410/660 km phase transitions in the mantle (Turcotte & Schubert, 2002), respectively. We use an isothermal slab because it is easier to control the magnitude of the negative buoyancy force acting on the system, especially when changing the subduction angle. The continental lithosphere on either side of the model consists of 15 km of upper crust, 15 km of lower crust and 70 km of lithospheric mantle (Figure 2). It is more buoyant than the oceanic slab and the underlying upper mantle. The geotherm of the continental lithosphere is described by a half-space cooling model with an age of 100 My. A sequence of passive margin sediments overlies the continental lithosphere on the side of the lower plate (Figure 2). The orogenic wedge is represented as a triangular shape made of sediments, extending 200 km from the subduction trench at 0 km (Figure 2). The rheological properties of the different model domains can be found in Table S1 in Supporting Information S1. The starting surface elevation is the same for all modeled subduction scenarios (Figure 2), serving as the initial basement topography for the SFMs.

In the GMs, we change (a) the initial subduction angle (Figure 2) and (b) the dislocation creep activation volume of the mantle (now referred to as activation volume). The former will control the magnitude of the downward-directed slab pull on the overlying surface (Capitanio et al., 2007; Forsyth & Uyeda, 1975; Stefanick & Jurdy, 1992), thereby providing direct feedback on the magnitude of isostatic rebound resulting from slab breakoff. The latter describes the dependence of the mantle viscosity on pressure (e.g., Poirier & Liebermann, 1984), based on which the upward buoyancy force and mantle traction counteracting the downward slab pull force may vary. Therefore, changing the activation volume directly influences the duration of slab necking and, thereby, the nature of isostatic rebound resulting from subsequent breakoff (Bercovici et al., 2015).

2.4.2. Stratigraphic Forward Models for Different Slab Breakoff Scenarios

Figure 3 shows the starting model configuration for the SFMs. Because we focus on the foreland basin, we take the central portion of our GMs as the model domain for our SFMs (Figure 2). This results in a 400 km wide model domain (Figure 3) divided into 200 cells, each 2 km wide. In the SFMs, the sea level remains constant as the basin floor experiences either subsidence or uplift. This means the presented models reflect the evolution of a foreland basin connected to the global seas rather than an isolated basin.

We refer to the slope of the foreland basin close to the mountain range as the proximal basin margin and the basinward side of the forebulge as the distal basin margin (Figure 3). The foreland basin is drowned up until the crest of the forebulge (Figure 3). The basement comprises 25% of four different sediment types: coarse sand, fine sand, silt, and clay (Figure 3 and Table S2 in Supporting Information S1). In GPM, we turn on the sediment diffusion, compaction, and tectonic processes, using the parameters specified in Table 2 and Figure 3. The diffusion coefficient used for calculating the diffusion rate (Equation 1) is based on a 2D cross-section of the NAFB from Lemcke (1988). Here, ~400 km^2 of sediments were deposited between 35 and 18 Ma during ongoing flexure of the European foreland plate. This results in an average diffusion coefficient of 22 m^2/yr (Table 2). The values for the diffusion curve ($C(z)$ in Equations 2 and 3, Figure 4a) are adjusted so that the sediment diffusion rates in either continental- or marine environments, as derived from Equations 2 and 3, match with those presented in literature (Nagel et al., 2018, their Table 6).

Table 2
Model Parameters Used in This Study

Parameter	Value	Unit
Width of model domain	400	km
Cell width	2	km
Method time increment	1	year
Base erodibility backbulge/forebulge/mountain range	0/0.001/0.25	n.d.
Active layer thickness (ALT)	0.4	m
Diffusion coefficient	22	m^2/yr
Contribution basement composition coarse sand/fine sand/silt/clay	25/25/25/25	%

Note. In all models the sediment type characteristics (Table S2 in Supporting Information S1) and diffusion curve (Figure 4a) are kept constant.

The ALT used in this study (0.4 m/yr, Table 2) is higher than observed erosion rates in nature (as high as 0.1 m/yr, Burbank, 2002; Herman et al., 2013; Montgomery & Brandon, 2002). However, we chose this value to account for the absence of a volumetric sediment source in our 2D models. This allowed us to obtain sedimentation rates in the synthetic foreland within the range observed in natural examples (0.015–2.15 mm/yr, Ballato et al., 2008; Burbank et al., 1988; DeCelles & Horton, 2003; Parra et al., 2010).

In models 90DF, 90DS, 60DF, 60DS, 45DF, 45DS, 30DF, and 30DS, all surface parameters (Table 2) are kept constant whilst the initial angle of subduction and mantle activation volume are altered (Table 3). In models 90DF-E and 90DS-E (Table 3), we introduce 50 m sea level changes with a period of 1 Myr (Figure 4b) to models 90DF and 90DS. This allows us to analyze whether third-order eustacy can mask the tectonostratigraphic signal from slab breakoff. Lastly, we conducted a sensitivity test for which the erodibility coefficient is set to 0.25 for all surface domains in the SFM (model 90DF-S, Table 3).

3. Results

In the following subsections, we describe the results of the reference model (Section 3.1), followed by an analysis of the effect of changes in the subduction angle (Section 3.2), mantle viscosity (Section 3.3), eustacy (Section 3.4), and foreland plate erodibility (Section 3.5) on the tectonostratigraphic signal from slab breakoff in a foreland basin.

Due to its low mantle viscosity, model 90DF is highly sensitive to changes in the slab pull force during slab necking- and breakoff. Therefore, it presents a good case to study expected changes in the foreland basin fill in the wake of these deep-seated processes.
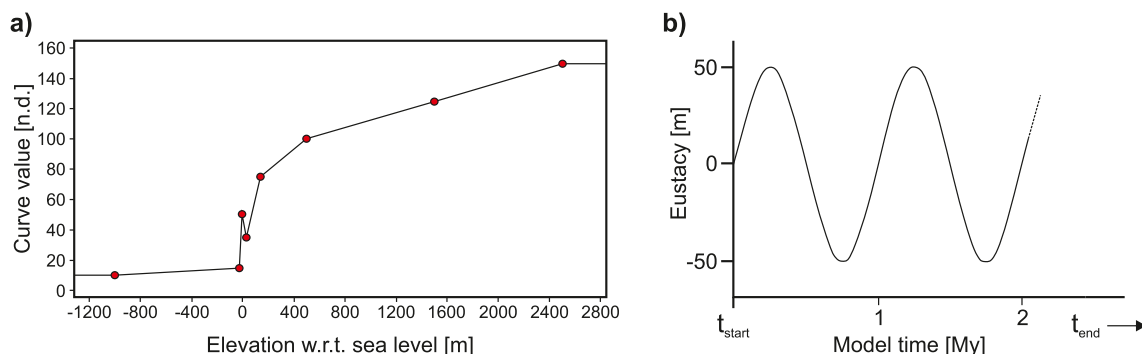

Figure 4. (a) Diffusion curve used in this study. (b) Eustacy for models 90DF-E and 90DS-E with an amplitude of 50 m and a period of 1 My.

Table 3
List of Simulations and Controlling Parameters Presented in This Study

Model name	Initial subduction angle [°]	Mantle dislocation activation volume [$\mu m^3 * mol^{-1}$]	Eustacy
90DF (reference)	90	8	No
60DF	60	8	No
45DF	45	8	No
30DF	30	8	No
90DS	90	12	No
60DS	60	12	No
45DS	45	12	No
30DS	30	12	No
90DF-E	90	8	Yes
90DS-E	90	12	Yes
90DF-S	90	8	No

3.1. Reference Model 90DF

During the reference model evolution (90DF, subduction angle 90° and activation volume 8 $\frac{\mu m^3}{mol}$, Table 1) we distinguish between four stages in the simulation; continental collision, slab necking, slab breakoff, and post breakoff (Figure 5). During the first stage, that is the first 0.81 Myr, the subducted oceanic slab hangs below the suture zone and controls the system by conducting a slab pull force to the surface (Figure 5a1). This leads to flexural subsidence of the lower plate and, thereby, the foreland basin with a rate of 3.2 km/Myr (Figure 5a3), generating accommodation space in the foreland at a rate of 0.25×10^{12} m^3/Myr (Figure 6e). Coevally, during this adjustment phase the mountain range is uplifted by up to 0.41 km/Myr (Figure 5a2) during which the sediment supply decreases from 4×10^{10} to 3.7×10^{10} m^3/Myr (Figure 6d). Sediments derived from the orogen are deposited in an underfilled, deep-water environment with an aggradational depositional trend (Figures 5a3 and 6a–6c). Furthermore, both basin margins are characterized by sediment bypass (Figures 5a3 and 6a–6c). In the synthetic seismic profile, these deposits are characterized by low-amplitude parallel reflectors (Figures 6f and 6g).

During the slab necking stage, thinning of the slab occurs at a depth of 120 km between 0.81 and 2.55 Myr of the model evolution (Figures 5b1 and 5c1) and is divided into an early and late phase. During early necking (until 2.43 Myr, Figure 5b1), foreland subsidence and mountain range uplift slow down (0.46 and 0.34 km/Myr, Figures 5b2 and 5b3). Therefore, the generation of accommodation space and sediment supply continues to decrease (0.1×10^{12} m^3/Myr, 3.46×10^{10} m^3/Myr, Figures 6d and 6e). As a result, the sediments do not record a change in basin architecture (Figures 6a–6c) and the seismic facies remains unchanged (Figures 6f and 6g). However, slab thinning accelerates during the late necking phase (from 2.43 to 2.55 Myr, Figure 5c1). This results in uplift of both the mountain range and the foreland with rates of 2.75 and 3.17 km/Myr, respectively (Figures 5c2 and 5c3). These lead to an increase in sediment supply of 2.6×10^{10} m^3/Myr (Figure 6d) and a negative rate in accommodation space generation of 1.6×10^{12} m^3/Myr (i.e., representing tectonic loss of accommodation space, Figure 6e), respectively. The rate at which the accommodation space reduces is two orders of magnitude higher than the increase in sediment supply. Furthermore, uplift of the proximal margin (Figure 3) causes this zone to become an area of sediment storage rather than bypass and/or erosion (Figure 5c3). Because of this, coarse-grained sediments are instead deposited on the proximal margin rather than being transported to the basin axis (Figure 6b). Coevally, the decreased sediment supply toward deeper environments results in the deposition of a condensed section in the basin axis.

During the slab breakoff stage, the oceanic slab detaches at a depth of 140 km after 2.58 Myr of model evolution (Figure 5d1). Consequently, short-lived (0.03 Myr, Figure 5d1) uplift of the foreland basin and mountain range occurs (25 and 30 km/Myr, Figures 5d2 and 5d3). The former forces a shallowing and related decrease in accommodation space with a rate of up to 3.7×10^{12} m^3/Myr (Figures 6a and 6e), the latter sediment supply increasing from 5.35×10^{10} m^3/Myr to a peak of 7.5×10^{10} m^3/Myr 0.1 Myr after slab breakoff (Figure 6d). From this moment
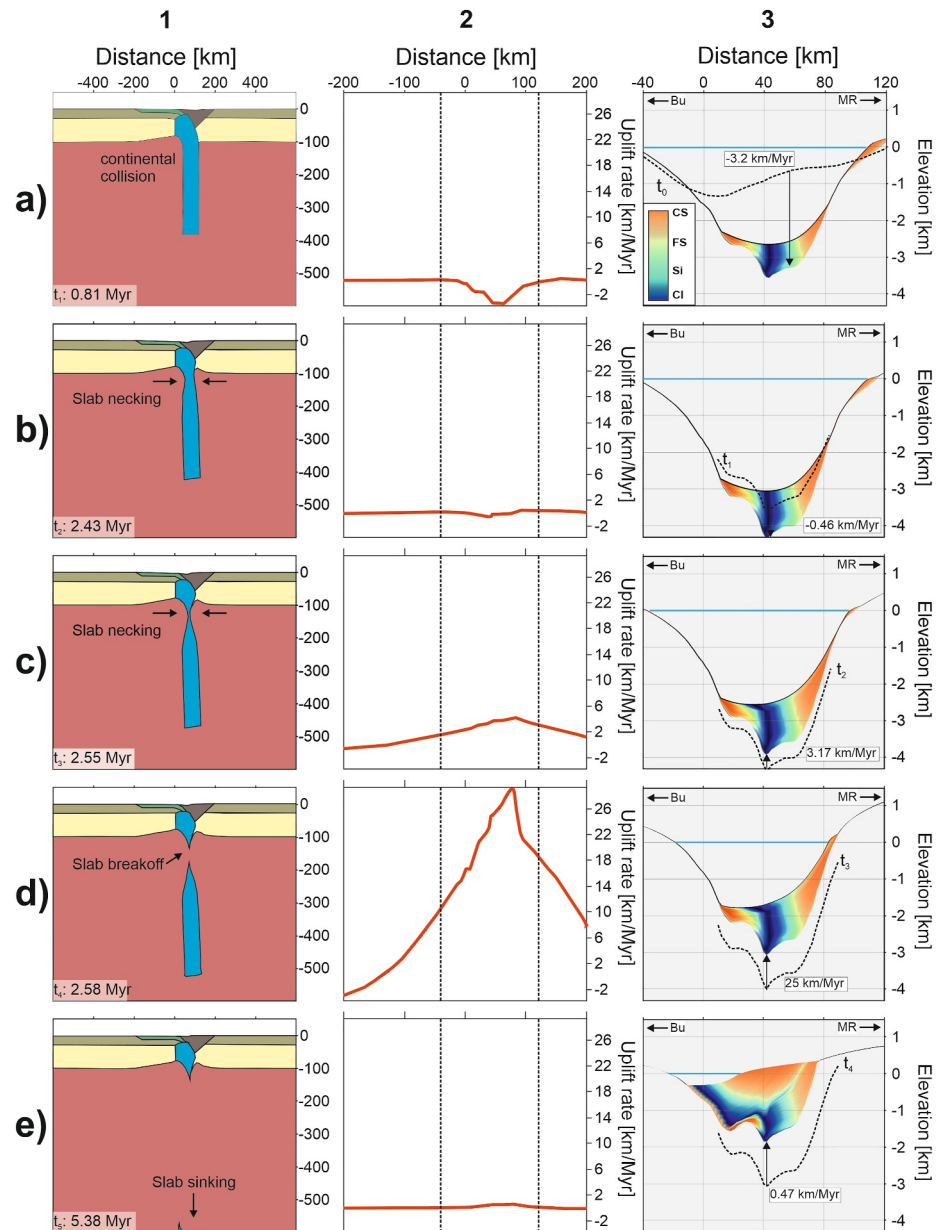
Figure 5. Evolution of model 90DF. Column 1 shows the geodynamic model evolution, column 2 the uplift (positive) and subsidence (negative) rates along the model domain, and column 3 the corresponding stratigraphic forward model (SFM) evolution. The vertical dashed lines in the uplift rate profiles indicate which area is visualized in column 3. The solid blue lines in the SFM indicates up until which level the basin is filled with water. The geodynamic models have the same color bar used in Figure 1. (a) Vertical subduction of the oceanic slab during continental collision (0.81 Myr); (b) initial phase of slab necking at a depth of 120 km coeval with subsidence of the foreland basin due to slab pull (2.43 Myr); (c) Last phase of slab necking causing isostatic rebound of foreland basin and mountain range (2.55 Myr); (d) slab breakoff at 120 km (2.58 Myr); (e) Slab sinking- and avalanching (5.38 Myr). CS = coarse sand, FS = fine sand, Si = silt, Cl = clay, MR = mountain range, Bu = forebulge.

onward, coarse-grained shallow water facies prograde over fine-grained facies on the proximal basin margin (Figures 6b and 6c). This causes a shallowing and progradation of the depositional facies (Figure 6c). Furthermore, this leads to an overall coarsening upward grading trend (Figure 6b), recorded on the proximal margin 0.7 Myr after breakoff (Figure 6c). In the synthetic seismic profile, this transition is recognized as a high amplitude reflector on the proximal margin defining the top of the syn-necking deposits (Figures 6f and 6g). The amplitude of this reflector decreases toward the basin axis (Figures 6f and 6g).
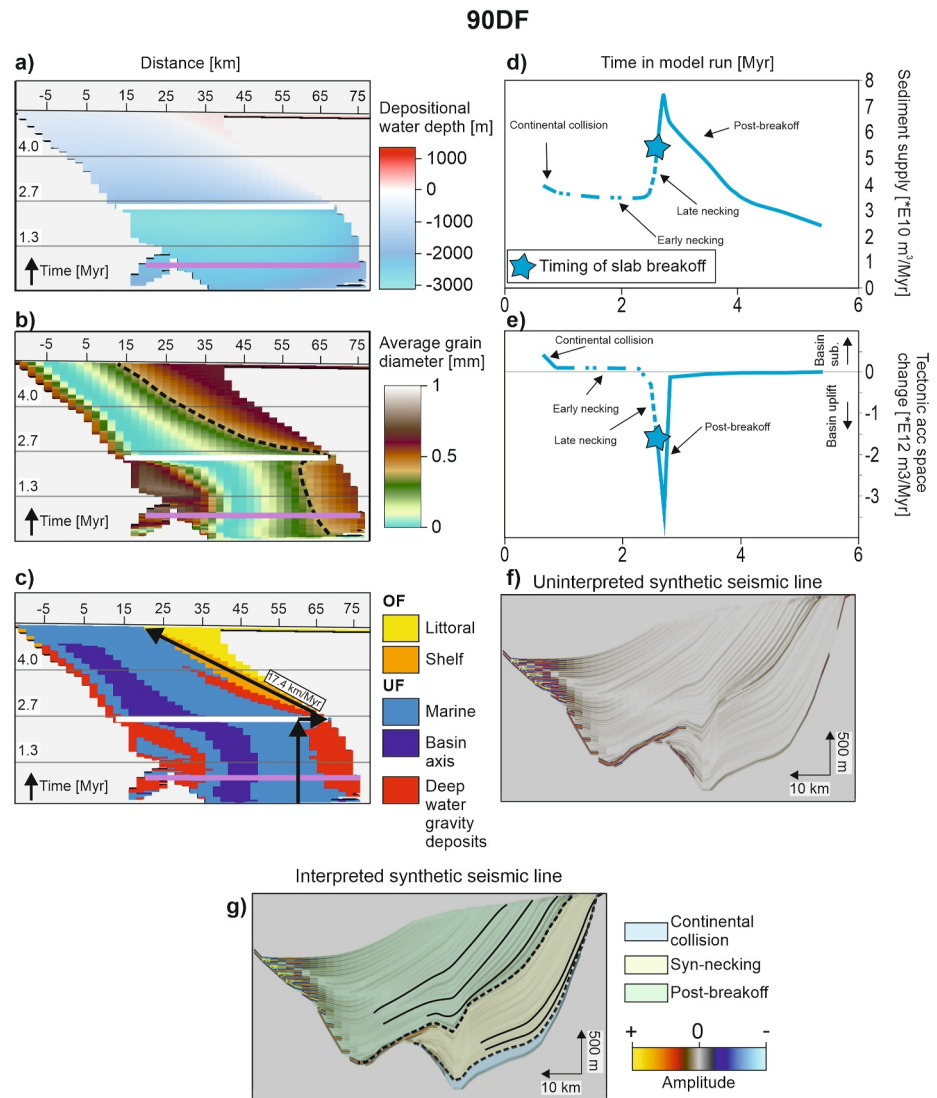
Figure 6. Reference model 90DF results. Purple horizontal lines in Wheeler diagrams indicate the onset of slab necking, white horizontal lines the timing of accelerated slab necking- and breakoff. (a) Wheeler diagram of the depositional water depth. (b) Wheeler diagram of the average grain size distribution. The black dashed line traces the coarse-grained sediment front (i.e., average grain size diameter ≥0.4 mm). (c) Wheeler diagram of the depositional environments. (d) Sediment supply over time. (e) The magnitude of tectonically created (positive) or destroyed (negative) accommodation space in the foreland basin. (f) Uninterpreted synthetic seismic section from model 90DF. (g) Interpreted synthetic seismic profile from model 90DF. OF = overfilled conditions, UF = underfilled conditions.

After breakoff, slab sinking (Figure 5e1) correlates with mountain range- and foreland basin surface uplift at rates of 0.32 and 0.44 km/Myr, respectively (Figures 5e2 and 5e3). However, the sediment supply decreases despite the mountain range uplift (Figure 6d). Furthermore, foreland basin uplift causes a loss of accommodation space at a rate which is 2–3 orders of magnitude lower compared to previous evolutionary stages (as low as 2.85×10^9 m^3/Myr, Figure 6e). Consequently, shallow water facies belt progrades into the basin axis and toward the distal margin at a constant rate of 17.4 km/Myr (Figures 3 and 6c). In the synthetic seismic profile this is recorded by low amplitude clinoforms prograding into the basin axis (Figures 6f and 6g).

3.2. Effect of Changing the Subduction Angle

In addition to the reference experiment, three models were created to test the influence of different subduction angles (60°, 45°, and 30°) while keeping mantle viscosity constant (models 60DF, 45DF, and 30DF, Table 3,

Figures S1–S3 in Supporting Information S1). In contrast to the vertical slab in the reference model, non-vertical slabs steepen while attached to the lower plate (Figures S1a1–S3a1 in Supporting Information S1). The slab with the shallowest initial subduction angle experiences the highest magnitude of steepening (28° for model 30DF, Figure S3a1 in Supporting Information S1), whereas it decreases for greater initial subduction angles to 11° (60DF, Figure S1a1 in Supporting Information S1). Likewise, lower initial subduction angles correlate with successively lower subsidence rates in the foreland basin in different models (3.2, 1.55, 1.42, and 1.16 km/Myr in the models 90DF, 60DF, 45DF, and 30DF, Figure 5a3; Figures S1a3, S2a3, and S3a3 in Supporting Information S1). In the case of higher initial subduction angles, the mountain range experiences uplift at a higher rate (0.41 and 0.24 km/Myr for models 90DF and 60DF, Figure 5a2 and Figure S1a1 in Supporting Information S1). In contrast, the mountain ranges subside at higher rates for lower initial subduction angles (0.18 and 1.33 km/Myr for models 45DF and 30DF, Figures S2b2 and S3b2 in Supporting Information S1). Subsidence of the mountain range in the two latter models results from dynamic subsidence as the shallow slabs steepen. In model 30DF, subsidence leads to submergence of the mountain range (Figure S3a2 in Supporting Information S1). Despite these differences, all models record the deposition of deep-water facies with an aggradational depositional trend in the basin axes (Figures S1a3 to S3a3 in Supporting Information S1). Grain size partitioning is recognized as low amplitude parallel reflectors in models with an initial subduction angle ≥45° (Figures 5a3 and 7d and Figures S1a3 and S2a3 in Supporting Information S1). In contrast, in model 30DF with a very low subduction angle, all grain sizes are mixed in a small depocenter (Figure S3a3 in Supporting Information S1), resulting in high amplitude parallel reflectors (Figure 7d).

During early slab necking, thinning of the slab occurs at progressively greater depths for shallower subduction angles (Figures S1b1–S3b1 in Supporting Information S1). Similarly, mountain range uplift rates during this phase decrease for lower subduction angles (0.2, 0.17, and 0.07 km/Myr for models 60DF, 45DF, and 30DF, Figures S1b2 to S3b2 in Supporting Information S1). Moreover, sediment supply generally decreases compared to the continent-continent collision stage (2.6×10^{10} and 1.44×10^{10} m³/Myr for 90DF and 60DF, Figure 8a) as erosion outpaces uplift during early slab necking. In contrast, models 45DF and 30DF record an increase in sediment supply instead (0.37×10^{10} and 0.1×10^{10} m³/Myr, Figure 8a). This occurs because the uplift rates outpace the denudation due to erosion. In model 30DF, sediments are trapped in the depression next to the foreland (resembling a wedge-top basin, Figure S3b2 in Supporting Information S1). The endmember models with the highest and lowest initial subduction angles (90DF and 30DF) record continued foreland basin subsidence during early slab necking (0.46 and 0.22 km/Myr, Figure 5b2 and Figure S3b2 in Supporting Information S1). In contrast, the intermediate cases (models 45DF and 60DF) record asymmetric uplift with decreasing rates for successively lower subduction angles (only the proximal margin is uplifted with 0.23 and 0.2 km/Myr for models 60DF and 45DF, Figures S1b3 and S2b3 in Supporting Information S1). In models 60DF and 45DF, this uplift results in a progradation of coarse-grained facies in a deep-water environment and related coarsening upward for models 60DF and 45DF (Figures 7b and 7c). This is expressed as a high-amplitude reflector at the top of the continental collision deposits in the synthetic seismic profile (Figure 7d).

Like in the reference model, the uplift of the mountain range and foreland occurs during the final stage of necking-and breakoff (Figures S1c1–S3c1 in Supporting Information S1). Uplift of the mountain range results in enhanced sediment supply (Figure 8a). Furthermore, these phases are also characterized by backstepping (representing a short phase of sediment starvation) and subsequent progradation and related coarsening-upward on the proximal basin margin in models 90DF, 60DF, and 45DF (Figures 7b and 7c). On the contrary, in model 30DF, this results in a progradational depositional trend (Figures 7b and 7c). In either case, this event is marked by a basin-wide high amplitude reflector at the top of the syn-necking deposits (Figure 7d). In the endmember models with the highest- and lowest initial subduction angles (90DF and 30DF), the basin records one overall coarsening-upward trend (Figure 7b). On the other hand, the intermediate initial subduction angle models (60DF and 45DF) record two coarsening-upward trends following early necking and the slab breakoff stages (Figure 7b). The lag time between the transition toward overfilled facies on the proximal margin and slab breakoff was 0.7, 1.3, and 2 Myr in models 90DF, 60DF, and 45DF (Figure 7c). In model 30DF, this transition does not occur (Figure 7c).

Slow continued uplift of both the mountain range and foreland basin during slab sinking (Figure 5e and Figures S1e–S3e in Supporting Information S1) do not induce rapid changes in basin architecture (Figure 7). Instead, shallow water facies continue to prograde into the basin axis and toward the distal margin at decreasing rates for initial lower subduction angles (17.4, 9.28, and 7.8 km/Myr for models 90DF, 60DF, and 45DF, Figure 7c). This is recognized in the synthetic seismic profiles as clinoforms prograding basinward (Figure 7d).
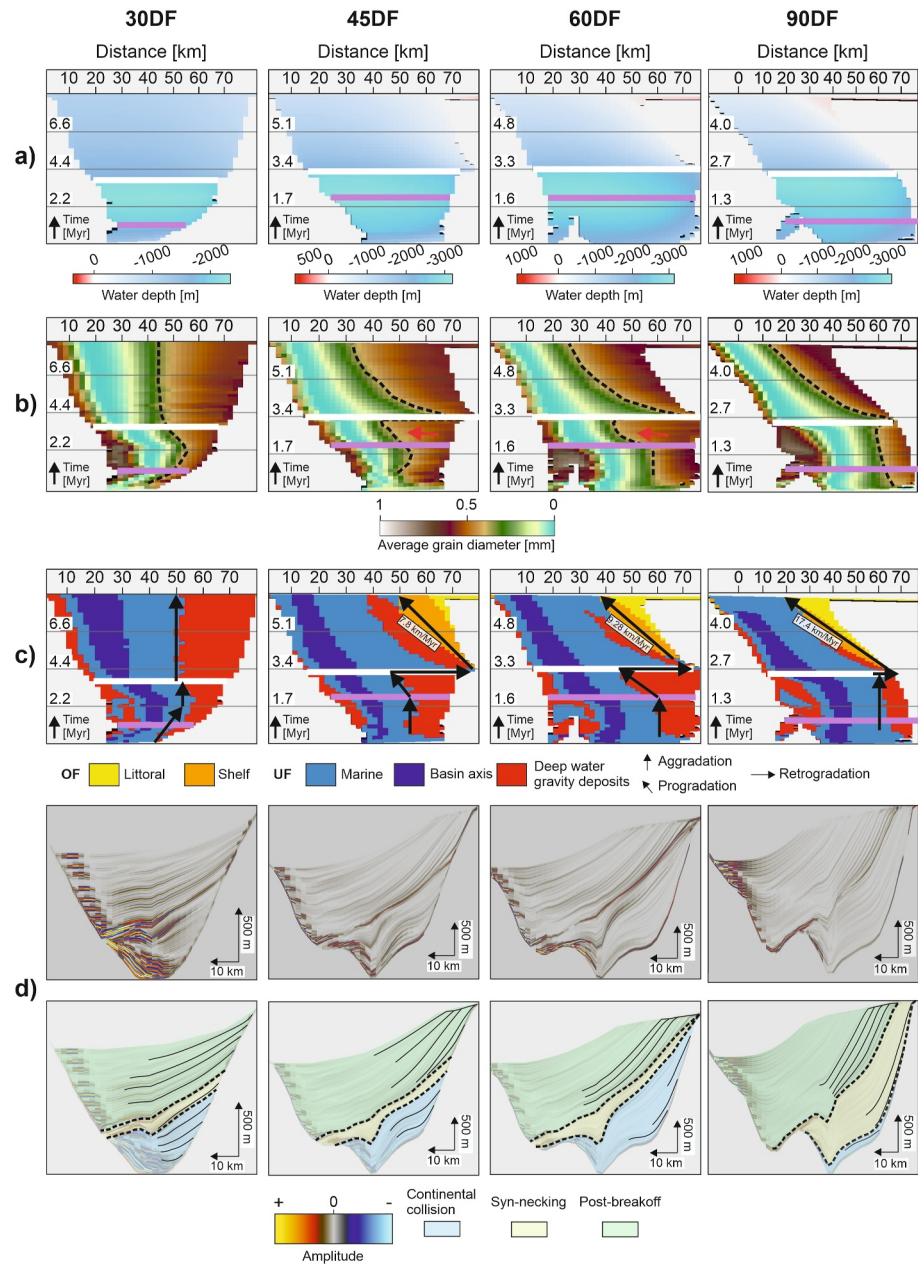
Figure 7. Results from models 30DF, 45DF, 60DF, and 90DF. Purple lines in Wheeler diagrams indicate the onset of slab necking, the white line the timing of accelerated slab necking- and breakoff. (a) Wheeler diagrams for the depositional water depth. (b) Wheeler diagrams for the average grain size distribution. The black dashed line traces the coarse-grained sediment front (i.e., average grain size diameter ≥0.4 mm). The red arrows for models 60DF and 45DF highlight progradation of deposition over an intrabasinal bump observed in Figures S1a3 and S2a3 in Supporting Information S1. A note to the reader is that this should not be mistaken for a stratigraphic signal of slab necking. (c) Wheeler diagrams for depositional facies. The basinward migration rate of overfilled conditions the values next to the black arrows. (d) Uninterpreted and interpreted synthetic seismics. The black dashed line in the interpreted version traces the reflectors that separates pre- and post-breakoff units.

3.3. Effect of Changing the Activation Volume

Increasing mantle viscosity, achieved by raising the activation volume from 8 to 12 $\frac{\mu m^3}{mol}$ for each simulation (models 90DS, 60DS, 45DS, and 30DS, Table 3), results in a lower magnitude of slab steepening during continental collision for non-vertical slabs (15–3°, Figures S5a1 to S7a1 in Supporting Information S1). Additionally,
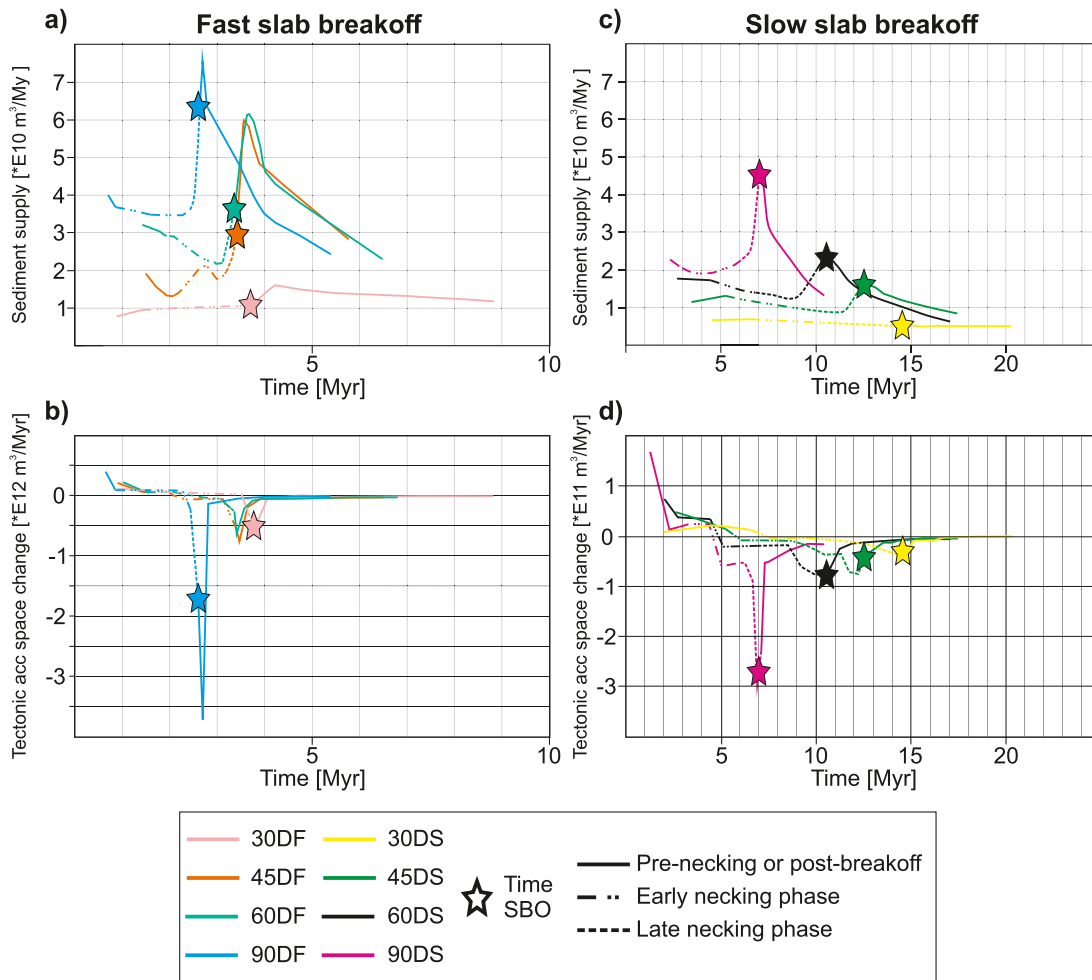
Figure 8. (a) Sediment supply rate changes for low mantle viscosity models. (b) Volume of accommodation space being generated (positive values) or lost (negative values) due to foreland basin subsidence- and uplift, respectively, for low mantle viscosity models. (c) Sediment supply rate changes for high mantle viscosity models. The dashed sections of the curves indicate ongoing slab necking. (d) Volume of accommodation space being generated (positive values) or destroyed (negative values) due to foreland basin subsidence- and uplift, respectively, for the high mantle viscosity models. SBO = slab breakoff.

mountain range uplift/subsidence rates (0.21, 0.07, 0.05, and −0.15 for models 90DS, 60DS, 45DS, and 30DS, Figures S4a2–S7a2 in Supporting Information S1) and foreland basin subsidence rates (1.06, 0.65, 0.6, and 0.27 km/Myr for models 90DS, 60DS, 45DS, and 30DS, Figures S4a3–S7a3 in Supporting Information S1) are lower compared to their low mantle viscosity counterparts. Like in model 30DF, the subsidence of the mountain range leads to submergence (Figure S7a2 in Supporting Information S1). Although thicker, deposition occurs in a deep-water environment with an aggradational trend in the basin axes concurrent with margin bypass (Figures 9a–9c and Figures S4a3–S7a3 in Supporting Information S1), like the low mantle viscosity models. Furthermore, the seismic facies of these deposits are the same (low amplitude parallel reflectors for models 90DS, 60DS, and 45DS and high amplitude parallel reflectors for model 30DS, Figure 9d).

During the necking- and breakoff stages, lower uplift rates for both the mountain range and foreland basins are recorded for models with a higher mantle viscosity (DS models, Table 3, Figures S4 to S7 in Supporting Information S1). The highest uplift rates are recorded during the late necking stage in the high mantle viscosity models (Figure S4c–S7c in Supporting Information S1). This is unlike the low mantle viscosity models, in which the highest uplift rates were recorded for slab breakoff rather than the late-stage necking (Figure 5 and Figures S1–S3 in Supporting Information S1). During this uplift, sediment supply increased in all models except 30DS (Figure 8c) in which topography was elevated only 150 m above sea level (Figure S7c2 in Supporting
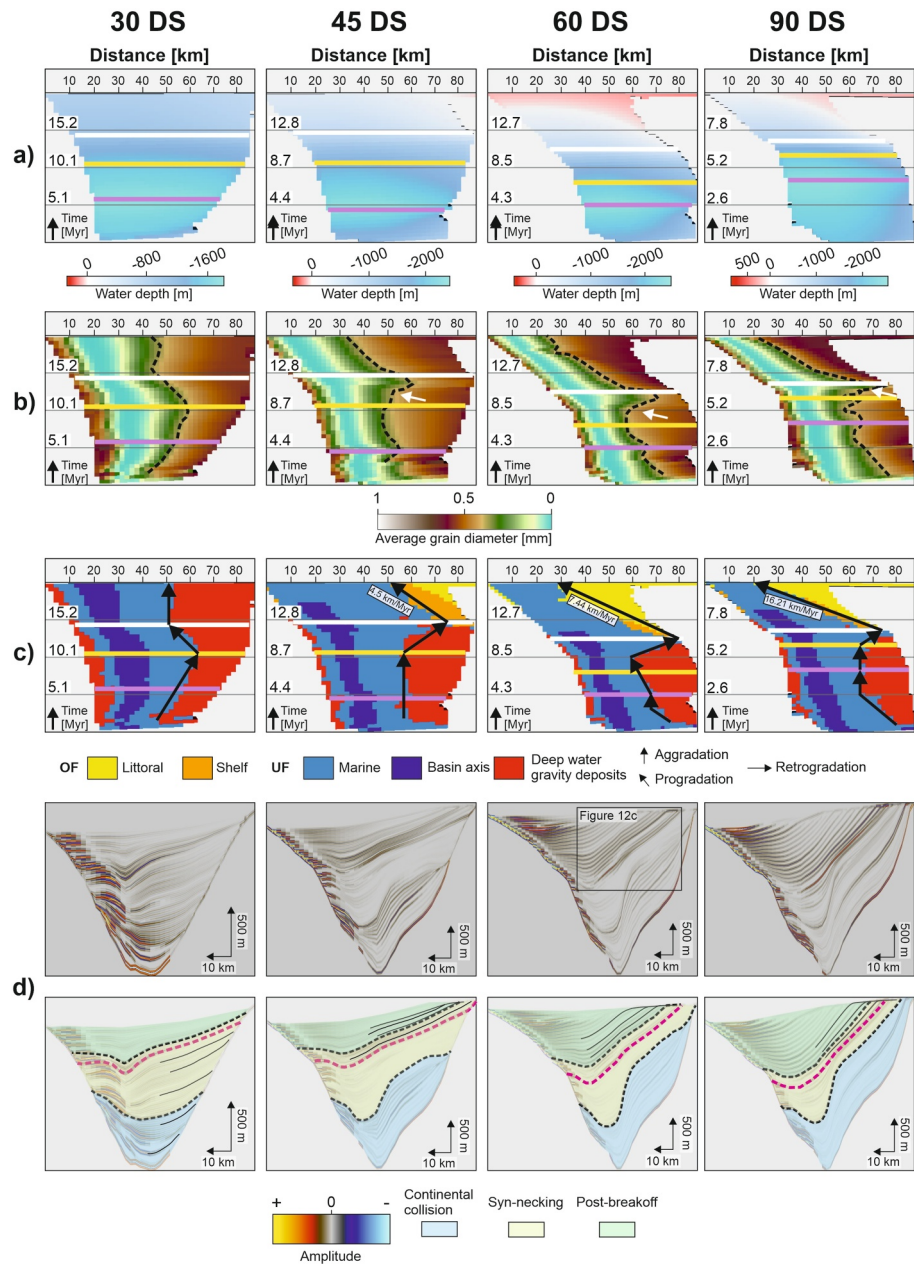
Figure 9. Results from models 30DS, 45DS, 60DS, and 90DS. Purple lines in Wheeler diagrams indicate the onset of slab necking, the yellow line the onset of accelerated slab necking, and the white line the timing of slab breakoff. (a) Wheeler diagrams for the depositional water depth. (b) Wheeler diagrams for the average grain size distribution. The black dashed line traces the coarse-grained sediment front (i.e., average grain size diameter ≥0.4 mm). White arrows highlight the retrogradation of coarse-grained deposition driven by necking-driven uplift of the proximal basin margin. (c) Wheeler diagrams for depositional facies. The time between slab breakoff and first shelf deposition is 0.4, 1.3, and 2.6 Myr after slab breakoff for models 90DS, 60DS, and 45DS, respectively. (d) Uninterpreted and interpreted synthetic seismics. Black dashed lines in the interpreted version trace the reflectors that separate pre-necking from the syn-necking and the syn-necking from the post-breakoff units. The purple dashed line indicates the onset of accelerated slab necking.

Information S1). Concurrent rates with which accommodation space decreased were one order of magnitude higher compared to sediment supply (Figures 8c and 8d).

The slab necking phase is prolonged, culminating in delayed slab breakoff in the high mantle viscosity models (difference up to 10.77 Myr for 30° initial subduction angle models, Figures S4d–S7d in Supporting

Information S1). Furthermore, instead of instantaneous backstepping of coarse-grained facies on the proximal margin in the low mantle viscosity models, this occurs over a time window of 1–2 Myr in the high mantle viscosity models (Figures 9b and 9c). This redistribution of grain sizes in the basin fill is expressed as a high-amplitude reflector within the syn-necking deposits (purple dashed lines in Figure 9d). This contrasts with the low mantle viscosity models where the final necking- and breakoff stage were condensed in a single reflector.

Although sediment supply decreases during protracted necking (Figure 8c), longer-lasting deposition allows for filling of the basins up until a point where water depths are less than 500 m at the proximal basin margin by the time breakoff occurs (Figure 9a and Figures S4d3–S7d3 in Supporting Information S1). As a result, there is virtually no lag time between the transition from the underfilled depositional facies to overfilled depositional facies on the proximal margin following slab breakoff in models 45DS, 60DS, and 90DS (Figure 9c). Like the low mantle viscosity models, necking- and breakoff do not force a similar transition in model 30DS (Figure 9c).

Slab sinking (Figure S4e1–S7e1 in Supporting Information S1) also induces uplift of the mountain range (0.04–0.13 km/Myr, Figures S4e2–S7e2 in Supporting Information S1) and foreland basin (0.02–0.17 km/Myr, Figures S4e3–S7e3 in Supporting Information S1). Like the low mantle viscosity models, these processes do not cause rapid changes in basin architecture and overfilled shallow water facies continue to prograde into the basin at a constant rate. However, these progradation rates are lower (16.21, 7.44, and 4.5 km/Myr for models 90DS, 60DS, and 45DS, Figure 9c) compared to their respective countermodels with a lower mantle viscosity. Despite the slower progradation rate, it is similarly expressed as high amplitude clinoforms prograding into the basin axis in the synthetic seismic profiles (Figure 9d).

3.4. Effect of Eustacy

In models 90DF-E and 90DS-E, eustatic sea level variations with an amplitude of 50 m and period of 1 Myr (Table 3, Figure 4b) were superimposed on the system as an external forcing parameter. In the pre-breakoff deposits, progradation and retrogradation of coarse-grained deep-water deposits over distances of up to 10 km can be observed (white and black arrows in Figures 10b and 10c). However, these features are not distinguishable in the synthetic seismic profiles (Figure 10d).

Like in the countermodels without eustacy (90DF and 90DS), necking and slab breakoff result in backstepping of coarse-grained underfilled deposition in the direction of the proximal basin margin (Figures 10b and 10c). This is subsequently followed by progradation of overfilled shallow water facies (Figures 10b and 10c). Some accelerations and decelerations can be observed for this progradation trend (green arrows in Figure 10c), recording the promotion- and slowdown of the progradation during a sea-level fall and rise, respectively. However, the overall change in basin architecture is similar to the models without eustacy. Moreover, these features cannot be observed in the synthetic seismic profiles (Figure 10d).

3.5. Symmetric Erodibility of the Mountain Range and Forebulge

Increased erodibility of the forebulge leads to more coarse-grained deposition at the base of the distal margin (Figure 11b) compared to the reference model 90DF. However, despite this difference, the seismic facies of the sediments deposited during continental collision and slab necking (low amplitude parallel reflectors, Figure 11d) is the same as that for the reference model. Progradation of overfilled, coarse-grained shallow water facies induced by slab necking- and breakoff has the same characteristics as in the reference model. However, uplift of the more erodible forebulge leads to a 2.6E10 m^3/Myr greater increase in sediment supply (Figure 11e). The extra volume of sediments derived from the forebulge are deposited downslope of the distal margin onto which mountain range-derived sediment onlap. This is expressed in the synthetic seismic profile as an intrabasinal unconformity (Figure 11d, yellow dashed line).

4. Discussion

In the following subsections, we will discuss the effects of varying parameters on a tectonostratigraphic signal of slab dynamics associated with the slab break-off process and its preservation potential in the foreland basin (Section 4.1). We then compare our synthetic models to natural examples suggested to have been influenced by slab breakoff to investigate whether first-order features observed in our models align with observations in these basins (Section 4.2). Lastly, we discuss the shortcomings of our models (Section 4.3).
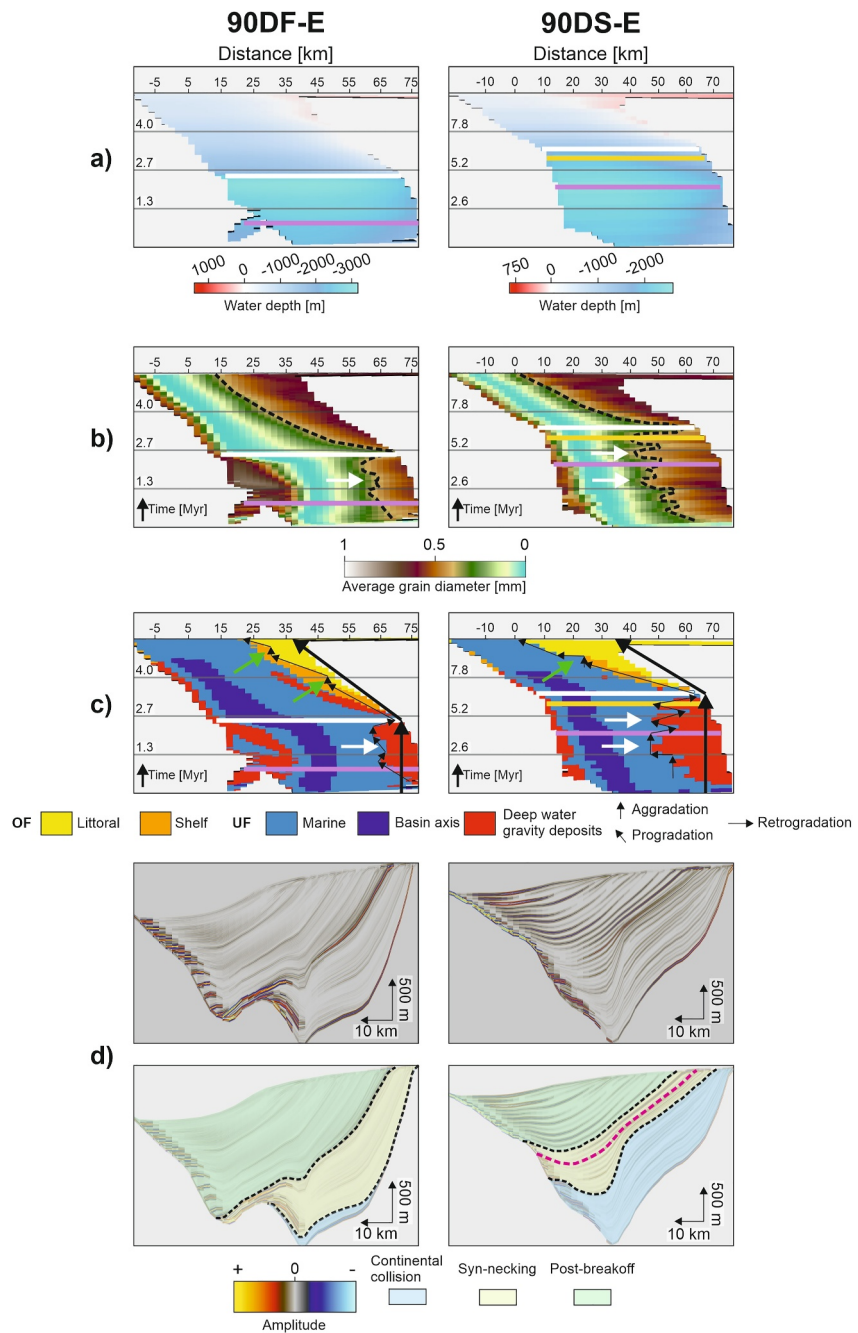
Figure 10. Models results from models 90DF-E and 90DS-E. Purple lines in Wheeler diagrams indicate the onset of slab necking, the white line the timing of slab breakoff. For model 90DS-E, the yellow line indicates the onset of accelerated slab necking. (a) Wheeler diagrams for the depositional water depth. (b) Wheeler diagrams for the average grain size distribution. The black dashed line traces the coarse-grained sediment front (i.e., average grain size diameter ≥0.4 mm). (c) Wheeler diagrams for depositional facies. Small black arrows indicate short-interval changes in depositional trend induced by eustacy, thick black arrows the overall basin-scale trend dictated by tectonics. (d) Uninterpreted and interpreted synthetic seismics. Black dashed lines in the interpreted version trace the reflectors that separate pre-necking from the syn-necking and the syn-necking from the post-breakoff units. For model 90DS-E, the purple dashed line indicates the onset of accelerated slab necking.
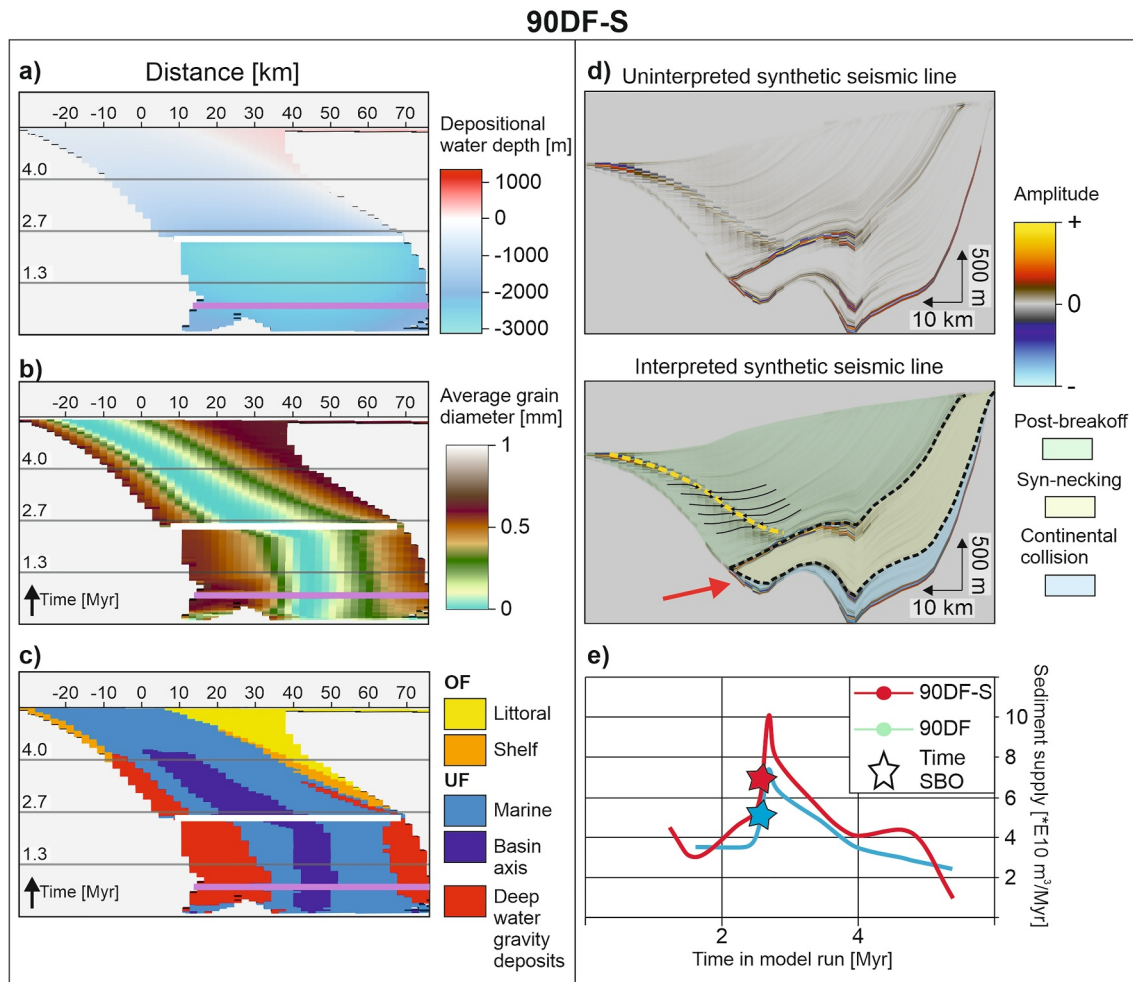
Figure 11. Models results from model 90DF-S. Purple lines in Wheeler diagrams indicate the onset of slab necking, the white line the timing of accelerated slab necking- and breakoff. (a) Wheeler diagrams for the depositional water depth. (b) Wheeler diagrams for the average grain size distribution. (c) Wheeler diagrams for depositional facies. (d) Uninterpreted and interpreted synthetic seismic profiles. Black dashed lines in the interpreted version traces the reflectors that separate pre-breakoff from the post-breakoff deposits. Yellow dashed line highlights the surface at which post-breakoff sediments derived from the mountain range onlap onto post-breakoff deposits derived from the forebulge.

4.1. Summary of the Numerical Results

4.1.1. The Tectonostratigraphic Signal of Slab Dynamics in a Foreland Basin

The continent-continent collision stage is associated with slab steepening, also exemplified in our results (Figures S1a1–S3a1 and S5a1–S7a1 in Supporting Information S1). Our models show that the magnitude of this steepening decreased for a higher (a) initial subduction angle and (b) mantle viscosity. The former can be explained by a higher initial subduction angle resulting in a lower torque acting on a slab (Lallemand et al., 2008, their Equation 3). The latter is attributed to a more viscous mantle providing greater buoyant support, inhibiting slab steepening. Previous studies demonstrated that slab steepening results in a dissipation of the pull force conducted to the surface (Capitanio et al., 2007; Di Giuseppe et al., 2009), with higher degrees of steepening expected to lead to greater dissipation. Because of this dissipation, the decrease in slab pull is greater for shallower dipping slabs after steepening. Subsequently, this results in a lower magnitude of slab pull being transmitted to the surface. This is expressed in our models as lower foreland basin subsidence rates for models with more shallow dipping slabs (Figure 5a3 and Figures S1a3–S3a3 in Supporting Information S1). Moreover, slabs subducting in a more viscous mantle experienced more buoyant support, leading to subsidence rates being one order of magnitude lower (Figures S4a3–S7a3 in Supporting Information S1). Likely, the high magnitude of steepening in the models with

an initial subduction angle of 30° was responsible for submergence of the mountain range independent from the mantle viscosity (Figures S3a3 and S7a3 in Supporting Information S1).

The subsequent slab necking was dynamic, accelerating in time (Figure 5 and Figures S1–S7 in Supporting Information S1). This was caused by the same pull force acting on an increasingly smaller area as the necking of the slab progressed. Consequently, slab necking- and breakoff induced reductions in slab pull transmitted to the surface. This in turn forced the uplift of the basin floor and mountain range through isostatic rebound, observed in our models as a decrease in accommodation space and enhanced sediment supply, respectively (Figure 8). Through this chain reaction, slab necking- and breakoff led to a transition from aggradational to progradational depositional trends and the transition from the underfilled facies to overfilled facies in the foreland basin (except for the 30° slab dip models, Figures 7b, 7c, 9b, and 9c). The rate of decrease in accommodation space was one to two orders higher compared to the enhanced sediment supply in the wake of isostatic rebound (Figure 8). Therefore, our models suggest basin floor uplift due to necking- and breakoff leading to isostatic rebound of the lower plate is likely the dominant cause for this transition.

The protracted necking stage in models with a high mantle viscosity resulted in a gradual transition, culminating in a thicker sedimentary sequence recording the change in basin architecture compared to the low mantle viscosity models (Figure 5 and Figures S1–S7 in Supporting Information S1). In the case of a low mantle viscosity, the system was more sensitive to the loss of slab pull during necking- and breakoff of slabs with different subduction angles. In our models, this is recorded as two coarsening upward cycles recorded within 2–3 Myr in models 60DF and 45DF; the first induced by the onset of slab necking and the second induced by breakoff (Figure 7b). In the case of high mantle viscosity, the higher shear force acting on the slab-mantle interface (Bercovici et al., 2015) decreases the rate at which slab pull reduces. Consequently, the related foreland basin- and mountain range uplift rates due to isostatic rebound of the foreland plate are lower for the high mantle viscosity models. As a result, the uplift rates and associated decrease in accommodation space and increase in sediment supply are only high enough during the final necking phase to force a backstepping-progradation in the high viscosity mantle models (Figures 9b and 9c). Therefore, only a single coarsening-upward cycle is recorded in these models (Figure 9b).

4.1.2. Masking of the Tectonostratigraphic Fingerprint of Slab Dynamics by Environmental Conditions

In the models in which eustacy was added (models 90DF-E and 90DS-E, Table 3), changes in sea level induced pro- and retrogradations of 10 km away from- and toward the proximal margin of the pre-breakoff deposits (Figures 10b and 10c). However, the overall architectural fingerprint of slab necking- and breakoff (i.e., facies belts rapidly migrating basinward) was not altered. Apart from the development of an intrabasinal unconformity in the post-breakoff fill in the distal part of the basin (Figure 11d), the tectonostratigraphic signal from slab necking- and breakoff in model 90DF-S did not change either. Furthermore, the resolution of the synthetic reflection seismic data in our models does not allow for the discerning of these eustacy-induced features (Figure 10d). However, these lateral km-scale features forced by eustacy may be observable at field-scale. In our models, these third-order eustatic sea level variations therefore represent "noise" on the scale of the overall basin evolution and are overshadowed by the tectonostratigraphic fingerprint of slab breakoff.

4.2. Comparison With a Natural Example and Implications

As emphasized in Section 2, simplifications in our modeling approach prohibit recreating fully natural scenarios while still allowing us to discern the first-order stratigraphic signal from slab breakoff in a foreland basin. Despite the introduced simplifications, we compare our model results to natural data to investigate whether the observed first-order changes in basin fill due to slab necking- and breakoff are also recorded in nature.

In our models with 30° initial subduction angles, the subdued mountain range topography was submerged during the continent-continent collision stage (Figures S3 and S7 in Supporting Information S1). Besides sedimentation in the foreland basin, this allowed for deposition in a wedge-top position. This is reminiscent of the deposition of the Augenstein Fm. in a wedge-top position in the Austrian Molasse, as suggested by previous authors (Hülscher et al., 2019; Schlunegger & Kissling, 2022).

However, the most striking feature of our models is the induced change from aggradational underfilled deposition to overfilled progradational deposition following slab necking- and breakoff. This transition is observed in many natural examples, and is attributed to increasing sediment supply, slab tearing- and breakoff, and/or eustacy (e.g.,
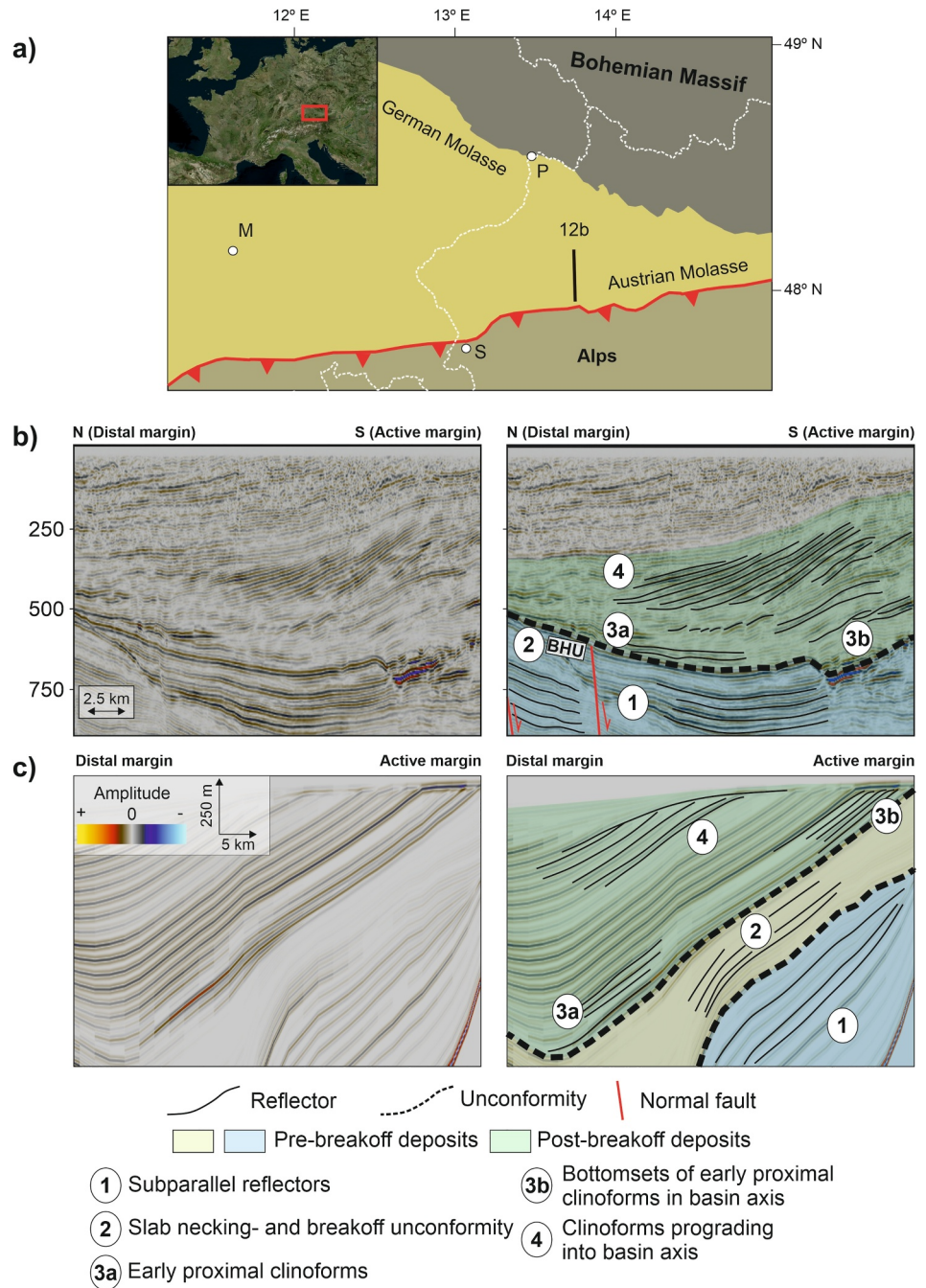
Figure 12. (a) Eastern Alps and the associated German- and Austrian Molasse Basin. M = Munich, P = Passau, S = Salzburg. (b) Uninterpreted (left) and interpreted (right) north south reflection seismic line through the Austrian Molasse, modified from Hülscher (2019). BHU = Basal Hall Unconformity. (c) Uninterpreted (left) and interpreted (right) synthetic reflection seismic line of model 60DS shown in Figure 9d.

Ascione et al., 2012; Lemcke, 1988; Meulenkamp et al., 1996; Sinclair, 1997). In the Austrian Molasse Basin (Figure 12a, Eastern NAFB), this transition is recorded as the stratigraphic upward transition from the deep-water Upper Puchkirchen Formation (1,000–1,500 m depositional water depth, Rögl et al., 1979) to the neritic- to littoral Hall Fm (<200 m depositional water depth at the top, Grunert et al., 2013; Hülscher et al., 2019) occurring at 19.6 to 18.3 Ma. In the reflection seismic data, this transition is imaged as the basin-wide high amplitude Basal Hall Unconformity overlain by prograding clinoforms (Figure 12b, Hülscher et al., 2019). This bears a

resemblance to the synthetic seismic profile from our model 60DS (Figure 12c). Moreover, Le Breton et al. (2023) reported a tectonically induced foreland basin uplift with a rate of 0.1–0.6 km/Myr that spatiotemporally correlates with a proposed slab breakoff below the Eastern Alps at 20 Ma (Handy, 2025; Handy et al., 2015; Schmid et al., 2004). This roughly matches with the uplift rate of 0.54 km/Myr observed for the model with a high mantle viscosity and initial subduction angle of 60° (60DS, Figure S5d3 in Supporting Information S1). Additionally, the increased sediment supply from the Eastern Alps around 20 Ma (Kuhlemann, 2000) might represent increased sediment supply due to necking- and breakoff induced uplift of the mountain range as recorded in model 60DS (Figure 8c). This implies that slab breakoff may have been a governing mechanism for the change from underfilled aggradational to progradational overfilled deposition, in agreement with previous authors (Schlunegger & Kissling, 2022). A similar chain reaction has been suggested to have occurred 10 Myrs earlier in the Central Alps (Garefalakis & Schlunegger, 2018; Schlunegger & Kissling, 2022; Sinclair, 1997).

However, uplift of the Eastern Alps after 20 Ma and the related enhanced sediment supply may alternatively be explained by the Alpine nappe stack overthrusting progressively thicker European lithosphere, inversion of Mesozoic structures on the Bohemian Spur, and indentation of the Eastern Alps by the Adriatic plate (Eskens et al., 2024; Favaro et al., 2015; Heberer et al., 2024; Le Breton et al., 2021). This implies that an increase in sediment supply forced by slab necking- and breakoff in our models is nonunique. Furthermore, following the model from Davies and von Blanckenburg (1995), slab breakoff below the Eastern Alps should have been paired with the intrusion of volcanics in the Eastern Alps around 20 Ma. Therefore, the lack of volcanics of this age in the Eastern Alps would argue against the occurrence of slab breakoff (Eskens et al., 2024). However, recent numerical studies suggest slab breakoff does not always result in intrusive magmatism (Freeburn et al., 2017). Though important, evaluating the link between a potential slab breakoff and (lack of) intrusive magmatism in the Eastern Alps at 20 Ma is not the focus of this contribution, and requires a dedicated study.

In the Betic Cordillera in southern Spain, the Serravallian to Messinian (predating the salinity crisis) evolution of sedimentary basins was coeval with lateral slab tearing of the Gibraltar Arc System (e.g., Chertova et al., 2014; Larrey et al., 2022; Spakman & Wortel, 2004). During this period, most of the basins recorded deepening, often associated with deep-water turbidites. This is subsequently followed by a rapid transition into shallow water ramp carbonate systems (e.g., Sorbas Basin, Andrić, Matenco, et al., 2018 and references therein), implying basin floor uplift rates between 0.3 and 0.6 km/Myr. This is reminiscent of the uplift rate from model 60DS (Figure S5 in Supporting Information S1). Alternatively, diachronous uplift of the Zagros foreland basin in the wake of slab breakoff- and tearing may have resulted in along-strike variations in thickness of syn-orogenic deposits (Koshnaw et al., 2024). The similarities between our model results natural analogs unveil that slab necking- and breakoff can force the onset of progradation of overfilled, non-condensed deposition in a foreland basin.

4.3. Model Limitations and Future Directions

The one-way coupled simulations presented in this study allowed characterization of the first-order tectonostratigraphic fingerprint from slab breakoff in a foreland basin. However, previous studies have demonstrated that erosion may induce isostatic uplift in a mountain range (Champagnac et al., 2009; Margirier et al., 2018; Paxman et al., 2016). Furthermore, the large influx of sediments due to slab breakoff may dampen the basin floor uplift from isostatic rebound in the foreland basin by enhancing the sedimentary load (DeCelles & Giles, 1996; Sinclair & Naylor, 2012). However, inherent to the one-way coupling approach used in this study, these dynamic interactions are not accounted for. Ideally, a two-way coupling between GMs and SFMs should be used to account for these interactions. However, this is beyond the scope of this contribution.

In many foreland basins, progressive overthrusting of the foreland plate leads to the basin fill either being overthrusted by- or incorporated into the orogenic wedge (e.g., Northern Alpine, Carpathian, and Guadalquivir foreland basins, Marín-Lechado et al., 2017; Marzec et al., 2018; Ortner et al., 2015). Furthermore, the onset of thrusting contributes to pulses of subsidence in the foreland basin and the basin-orthogonal migration of facies (Flemings & Jordan, 1990). However, previous authors suggested slab breakoff may induce a decrease in plate convergence rates (Ferrari, 2004; Ma et al., 2014; Zhu et al., 2017). Therefore, the tectonostratigraphic signal from slab breakoff will likely not be overprinted by ongoing overthrusting of the foreland. Furthermore, the uplift due to breakoff (Buiter et al., 2002; Fernández-García et al., 2019; van Hunen and Allen, 2011) will likely overshadow other coevally operating processes. This is especially expected in the case of subduction orogens

where the thrust belts are mainly controlled by the slab-pull (Appenines, Carpathians, Dinarides, Betic Corrdilera, and Hellenides, Andrić, Vogt, et al., 2018; Royden & Faccenna, 2018). This is compatible with both our results (Section 4.1) and the evolution of the Apennines (Lanari et al., 2023).

Lastly, our models only consider the effect of slab breakoff on the tectonostratigraphic development of a foreland basin in 2D. However, many natural examples of foreland basins record along-strike architectural variations (e.g., Northern Alpine, Appalachian, Apenninic, and Tarim foreland basins, Amadori et al., 2019; He et al., 2016; Lash, 1988; Lemcke, 1988), potentially induced by lateral slab tearing (Meulenkamp et al., 1996; Van der Meulen et al., 1998). Therefore, we suggest expanding the presented research to 3D to quantitatively investigate this hypothesis.

5. Conclusions

In this study we combined 2D GMs with SFMs, allowing us to quantitatively approximate the first-order tectonostratigraphic signal from slab necking- and breakoff in a foreland basin. Model results exemplify that before slab necking initiates, the lithosphere of the lower plate accommodates the pull force through flexural subsidence. This phase is characterized by deep-water deposition with an aggradational trend. However, during slab necking- and breakoff, the progressively faster decrease in slab pull conducted to the surface results in uplift of the foreland basin- and mountain range. These cause the accommodation space to tectonically decrease through basin floor uplift and the sediment supply to increase due to mountain range uplift, respectively. Together, these processes cause a shift from aggradational to progradational deposition, and the basin fill transitioning from underfilled facies- to an overfilled facies. The rate at which accommodation space tectonically diminishes is greater than sediment supply increases. Therefore, basin floor uplift due to isostatic rebound of the foreland plate is of first-order importance for this transition, and sediment supply increases of second order. In the case of low mantle viscosity, the system is more sensitive to the loss of slab pull. This led to condensation of the necking- and breakoff stages and their respective tectonostratigraphic signals. In contrast, in a viscous mantle only the uplift rates during final necking are ample to induce changes in grain size distribution and increases in sediment supply to force a change in basin architecture. Lastly, environmental conditions in the form of eustacy and erodibility cannot mask the tectonostratigraphic signal from slab necking- and breakoff in our parameter space.

In our models, the slab necking- and breakoff induced a transition from aggradational underfilled deposition to overfilled progradational deposition. This was recorded as a high amplitude reflector overlain by prograding clinoforms. In the Austrian Molasse, a similar sequence records the transition from deep marine deposition toward shallow marine prograding sedimentation, spatiotemporally correlating with suggested slab breakoff under the Eastern Alps. Therefore, our models support the hypothesis that this transition in the Austrian Molasse may have been induced by slab breakoff. Moreover, our model setups are also applicable to slab pull-driven orogen-foreland systems, such as the Appenines, Carpathians, Dinarides, Hellenides, and Betic Cordillera.

Conflict of Interest

The authors declare no conflicts of interest relevant to this study.

Data Availability Statement

The code in which the 2D thermomechanical models were constructed (LaMEM) is open-source and can freely be downloaded from https://github.com/UniMainzGeo/LaMEM. Input files to for the geodynamic simulations and.hdf5 and.json files to rerun the geodynamic- and stratigraphic forward models presented in this study are uploaded at https://zenodo.org/records/15402334 (Eskens et al., 2025). CorelDraw 2021 was used for post-processing to make the figures presented in this study. Figure 12a was redrawn in accordance to https://creativecommons.org/licenses/by/4.0/. For an academic Petrel license including GPM SLB must be contacted.

References

Afonso, J. C., Fernandez, M., Ranalli, G., Griffin, W., & Connolly, J. (2008). Integrated geophysical-petrological modeling of the lithosphere and sublithospheric upper mantle: Methodology and applications. *Geochemistry, Geophysics, Geosystems*, 9(5), Q05008. https://doi.org/10.1029/2007gc001834

Allen, J. (1965). Late Quaternary Niger delta, and adjacent areas: Sedimentary environments and lithofacies. *AAPG Bulletin*, 49(5), 547–600. https://doi.org/10.1306/a663363a-16c0-11d7-8645000102c1865d

Amadori, C., Toscani, G., Di Giulio, A., Maesano, F. E., D'Ambrogi, C., Ghielmi, M., & Fantoni, R. (2019). From cylindrical to non-cylindrical foreland basin: Pliocene–pleistocene evolution of the Po Plain–Northern adriatic basin (Italy). *Basin Research*, *31*(5), 991–1015. https://doi.org/10.1111/bre.12369

Andrews, E. R., & Billen, M. I. (2009). Rheologic controls on the dynamics of slab detachment. *Tectonophysics*, *464*(1–4), 60–69. https://doi.org/10.1016/j.tecto.2007.09.004

Andrić, N., Matenco, L., Hilgen, F., & de Bresser, H. (2018). Structural controls on sedimentation during asymmetric extension: The case of Sorbas Basin (SE Spain). *Global and Planetary Change*, *171*, 185–206. https://doi.org/10.1016/j.gloplacha.2018.01.019

Andrić, N., Vogt, K., Matenco, L., Cvetković, V., Cloetingh, S., & Gerya, T. (2018). Variability of orogenic magmatism during Mediterranean-style continental collisions: A numerical modelling approach. *Gondwana Research*, *56*, 119–134. https://doi.org/10.1016/j.gr.2017.12.007

Ascione, A., Ciarcia, S., Di Donato, V., Mazzoli, S., & Vitale, S. (2012). The Pliocene-Quaternary wedge-top basins of southern Italy: An expression of propagating lateral slab tear beneath the Apennines. *Basin Research*, *24*(4), 456–474. https://doi.org/10.1111/j.1365-2117.2011.00534.x

Ballato, P., Nowaczyk, N. R., Landgraf, A., Strecker, M. R., Friedrich, A., & Tabatabaei, S. H. (2008). Tectonic control on sedimentary facies pattern and sediment accumulation rates in the Miocene foreland basin of the southern Alborz mountains, northern Iran. *Tectonics*, *27*(6), TC6001. https://doi.org/10.1029/2008tc002278

Baumann, C., Gerya, T. V., & Connolly, J. A. (2010). Numerical modelling of spontaneous slab breakoff dynamics during continental collision. *Geological Society*, *332*(1), 99–114. https://doi.org/10.1144/sp332.7

Beaumont, C. (1981). Foreland basins. *Geophysical Journal International*, *65*(2), 291–329. https://doi.org/10.1111/j.1365-246x.1981.tb02715.x

Bercovici, D., Schubert, G., & Ricard, Y. (2015). Abrupt tectonics and rapid slab detachment with grain damage. *Proceedings of the National Academy of Sciences*, *112*(5), 1287–1291. https://doi.org/10.1073/pnas.1415473112

Boussinesq, J. (1897). *Théorie de l'écoulement tourbillonnant et tumultueux des liquides dans les lits rectilignes à grande section, 1*. Gauthier-Villars.

Buiter, S. J., Govers, R., & Wortel, M. (2002). Two-dimensional simulations of surface deformation caused by slab detachment. *Tectonophysics*, *354*(3–4), 195–210. https://doi.org/10.1016/s0040-1951(02)00336-0

Burbank, D. (2002). Rates of erosion and their implications for exhumation. *Mineralogical Magazine*, *66*(1), 25–52. https://doi.org/10.1180/0026461026610014

Burbank, D., Beck, R., Raynolds, R., Hobbs, R., & Tahirkheli, R. (1988). Thrusting and gravel progradation in foreland basins: A test of post-thrusting gravel dispersal. *Geology*, *16*(12), 1143–1146. https://doi.org/10.1130/0091-7613(1988)016<1143:tagpif>2.3.co;2

Burov, E., & Yamato, P. (2008). Continental plate collision, p–t–t–z conditions and unstable vs. stable plate dynamics: Insights from thermo-mechanical modelling. *Lithos*, *103*(1–2), 178–204. https://doi.org/10.1016/j.lithos.2007.09.014

Capitanio, F. A., Morra, G., & Goes, S. (2007). Dynamic models of downgoing plate-buoyancy driven subduction: Subduction motions and energy dissipation. *Earth and Planetary Science Letters*, *262*(1–2), 284–297. https://doi.org/10.1016/j.epsl.2007.07.039

Catuneanu, O. (2004). Basement control on flexural profiles and the distribution of foreland facies: The Dwyka Group of the Karoo Basin, South Africa. *Geology*, *32*(6), 517–520. https://doi.org/10.1130/g20526.1

Catuneanu, O., Galloway, W. E., Kendall, C. G. S. C., Miall, A. D., Posamentier, H. W., Strasser, A., & Tucker, M. E. (2011). Sequence stratigraphy: Methodology and nomenclature. *Newsletters on Stratigraphy*, *44*(3), 173–245. https://doi.org/10.1127/0078-0421/2011/0011

Champagnac, J.-D., Schlunegger, F., Norton, K., von Blanckenburg, F., Abbühl, L. M., & Schwab, M. (2009). Erosion-driven uplift of the modern Central Alps. *Tectonophysics*, *474*(1–2), 236–249. https://doi.org/10.1016/j.tecto.2009.02.024

Chertova, M., Spakman, W., Geenen, T., Van Den Berg, A., & Van Hinsbergen, D. (2014). Underpinning tectonic reconstructions of the western Mediterranean region with dynamic slab evolution from 3-D numerical modeling. *Journal of Geophysical Research: Solid Earth*, *119*(7), 5876–5902. https://doi.org/10.1002/2014jb011150

Covey, M. (1986). The evolution of foreland basins to steady state: Evidence from the western Taiwan foreland basin. *Foreland basins*, 77–90. https://doi.org/10.1002/9781444303810.ch4

Croissant, T., Steer, P., Lague, D., Davy, P., Jeandet, L., & Hilton, R. G. (2019). Seismic cycles, earthquakes, landslides and sediment fluxes: Linking tectonics to surface processes using a reduced-complexity model. *Geomorphology*, *339*, 87–103. https://doi.org/10.1016/j.geomorph.2019.04.017

DeCelles, P. G. (2012). Foreland basin systems revisited: Variations in response to tectonic settings. *Tectonics of sedimentary basins: Recent advances*, 405–426. https://doi.org/10.1002/9781444347166.ch20

DeCelles, P. G., & Giles, K. A. (1996). Foreland basin systems. *Basin Research*, *8*(2), 105–123. https://doi.org/10.1046/j.1365-2117.1996.01491.x

DeCelles, P. G., & Horton, B. K. (2003). Early to middle tertiary foreland basin development and the history of Andean crustal shortening in Bolivia. *Geological Society of America Bulletin*, *115*(1), 58–77. https://doi.org/10.1130/0016-7606(2003)115<0058:etmtfb>2.0.co;2

Diem, B. (1986). Die Untere Meeresmolasse zwischen der Saane (Westschweiz) und der Ammer (Oberbayern). *Eclogae Geologicae Helvetiae*, *79*(2), 493–559.

Di Giuseppe, E., Faccenna, C., Funiciello, F., van Hunen, J., & Giardini, D. (2009). On the relation between trench migration, seafloor age, and the strength of the subducting lithosphere. *Lithosphere*, *1*(2), 121–128. https://doi.org/10.1130/l26.1

Duretz, T., Gerya, T. V., & May, D. A. (2011). Numerical modelling of spontaneous slab breakoff and subsequent topographic response. *Tectonophysics*, *502*(1–2), 244–256. https://doi.org/10.1016/j.tecto.2010.05.024

Duretz, T., Schmalholz, S., & Gerya, T. (2012). Dynamics of slab detachment. *Geochemistry, Geophysics, Geosystems*, *13*(3), Q03020. https://doi.org/10.1029/2011gc004024

Ehlers, T. A., & Poulsen, C. J. (2009). Influence of Andean uplift on climate and paleoaltimetry estimates. *Earth and Planetary Science Letters*, *281*(3–4), 238–248. https://doi.org/10.1016/j.epsl.2009.02.026

Eskens, L. H., Andrić-Tomašević, N., Süss, P. M., Müller, M., Herrmann, R., & Ehlers, T. A. (2024). Lithospheric-and crustal-scale controls on variations in foreland basin development in the Northern Alpine Foreland Basin. *Tectonophysics*, *878*, 230283. https://doi.org/10.1016/j.tecto.2024.230283

Eskens, L. H., Thielmann, M., Piccolo, A., Claussmann, B., Lejri, M., Ehlers, T. A., & Andrić-Tomašević, N. (2025). The tectonostratigraphic expression of slab breakoff in foreland basins: Insights from 2D forward stratigraphic modeling [Dataset]. https://zenodo.org/records/15402334.Tectonics

Favaro, S., Schuster, R., Handy, M. R., Scharf, A., & Pestal, G. (2015). Transition from orogen-perpendicular to orogen-parallel exhumation and cooling during crustal indentation—Key constraints from 147Sm/144Nd and 87Rb/87Sr geochronology (Tauern Window, Alps). *Tectonophysics*, *665*, 1–16. https://doi.org/10.1016/j.tecto.2015.08.037

Fernández-García, C., Guillaume, B., & Brun, J.-P. (2019). 3D slab breakoff in laboratory experiments. *Tectonophysics*, *773*, 228223. https://doi.org/10.1016/j.tecto.2019.228223

Ferrari, L. (2004). Slab detachment control on mafic volcanic pulse and mantle heterogeneity in central Mexico. *Geology*, *32*(1), 77–80. https://doi.org/10.1130/g19887.1

Flemings, P. B., & Jordan, T. E. (1989). A synthetic stratigraphic model of foreland basin development. *Journal of Geophysical Research*, *94*(B4), 3851–3866. https://doi.org/10.1029/jb094ib04p03851

Flemings, P. B., & Jordan, T. E. (1990). Stratigraphic modeling of foreland basins: Interpreting thrust deformation and lithosphere rheology. *Geology*, *18*(5), 430–434. https://doi.org/10.1130/0091-7613(1990)018<0430:smofbi>2.3.co;2

Forsyth, D., & Uyeda, S. (1975). On the relative importance of the driving forces of plate motion. *Geophysical Journal International*, *43*(1), 163–200. https://doi.org/10.1111/j.1365-246x.1975.tb00631.x

Freeburn, R., Bouilhol, P., Maunder, B., Magni, V., & van Hunen, J. (2017). Numerical models of the magmatic processes induced by slab breakoff. *Earth and Planetary Science Letters*, *478*, 203–213. https://doi.org/10.1016/j.epsl.2017.09.008

Garefalakis, P., & Schlunegger, F. (2018). Link between concentrations of sediment flux and deep crustal processes beneath the European Alps. *Scientific Reports*, *8*(1), 183. https://doi.org/10.1038/s41598-017-17182-8

Gerya, T. V., Yuen, D. A., & Maresch, W. V. (2004). Thermomechanical modelling of slab detachment. *Earth and Planetary Science Letters*, *226*(1–2), 101–116. https://doi.org/10.1016/j.epsl.2004.07.022

Grunert, P., Hinsch, R., Sachsenhofer, R. F., Bechtel, A., Ćorić, S., Harzhauser, M., et al. (2013). Early Burdigalian infill of the Puchkirchen trough (North Alpine Foreland Basin, Central Paratethys): Facies development and sequence stratigraphy. *Marine and Petroleum Geology*, *39*(1), 164–186. https://doi.org/10.1016/j.marpetgeo.2012.08.009

Handy, M. R. (2025). Orogenic structure and topography track subduction singularities during slab delemination and detachment. *Scientific Reports*, *15*(1), 12091. https://doi.org/10.1038/s41598-025-94789-2

Handy, M. R., Ustaszewski, K., & Kissling, E. (2015). Reconstructing the alps–carpathians–dinarides as a key to understanding switches in subduction polarity, slab gaps and surface motion. *International Journal of Earth Sciences*, *104*(1), 1–26. https://doi.org/10.1007/s00531-014-1060-3

He, B., Jiao, C., Xu, Z., Cai, Z., Zhang, J., Liu, S., et al. (2016). The paleotectonic and paleogeography reconstructions of the Tarim Basin and its adjacent areas (NW China) during the late early and Middle Paleozoic. *Gondwana Research*, *30*, 191–206. https://doi.org/10.1016/j.gr.2015.09.011

Heberer, B., Salcher, B. C., Tari, G., Wessely, G., Dunkl, I., Sachsenhofer, R. F., et al. (2024). The impact of the Bohemian Spur on the cooling and exhumation pattern of the Eastern Alpine wedge of the European Alps. *Tectonics*, *43*(3), e2023TC008005. https://doi.org/10.1029/2023tc008005

Herman, F., Seward, D., Valla, P. G., Carter, A., Kohn, B., Willett, S. D., & Ehlers, T. A. (2013). Worldwide acceleration of mountain erosion under a cooling climate. *Nature*, *504*(7480), 423–426. https://doi.org/10.1038/nature12877

Holt, A., Royden, L., & Becker, T. (2017). The dynamics of double slab subduction. *Geophysical Journal International*, *209*(1), 250–265.

Hülscher, J., Fischer, G., Grunert, P., Auer, G., & Bernhardt, A. (2019). Selective recording of tectonic forcings in an Oligocene/Miocene submarine channel system: Insights from new age constraints and sediment volumes from the Austrian Northern Alpine Foreland Basin. *Frontiers in Earth Science*, *7*, 302. https://doi.org/10.3389/feart.2019.00302

Isacks, B., & Molnar, P. (1969). Mantle earthquake mechanisms and the sinking of the lithosphere. *Nature*, *223*(5211), 1121–1124. https://doi.org/10.1038/2231121a0

Jordan, T. E. (1981). Thrust loads and foreland basin evolution, Cretaceous, western United States. *AAPG Bulletin*, *65*(12), 2506–2520. https://doi.org/10.1306/03b599f4-16d1-11d7-8645000102c1865d

Jordan, T. E., & Flemings, P. (1991). Large-scale stratigraphic architecture, eustatic variation, and unsteady tectonism: A theoretical evaluation. *Journal of Geophysical Research*, *96*(B4), 6681–6699. https://doi.org/10.1029/90jb01399

Kaus, B. J., Popov, A. A., Baumann, T., Pusok, A., Bauville, A., Fernandez, N., & Collignon, M. (2016). Forward and inverse modelling of lithospheric deformation on geological timescales. In *NIC symposium* (pp. 299–307).

Koshnaw, R. I., Kley, J., & Schlunegger, F. (2024). The Miocene subsidence pattern of the NW Zagros foreland basin reflects the southeastward propagating tear of the Neotethys slab. *Solid Earth*, *15*(11), 1365–1383. https://doi.org/10.5194/se-15-1365-2024

Kufner, S. K., Kakar, N., Bezada, M., Bloch, W., Metzger, S., Yuan, X., et al. (2021). The Hindu Kush slab break-off as revealed by deep structure and crustal deformation. *Nature Communications*, *12*(1), 1685. https://doi.org/10.1038/s41467-021-21760-w

Kufner, S.-K., Schurr, B., Haberland, C., Zhang, Y., Saul, J., Ischuk, A., & Oimahmadov, I. (2017). Zooming into the Hindu Kush slab break-off: A rare glimpse on the terminal stage of subduction. *Earth and Planetary Science Letters*, *461*, 127–140. https://doi.org/10.1016/j.epsl.2016.12.043

Kuhlemann, J. (2000). Post-collisional sediment budget of circum-alpine basins (Central Europe). *Memories Science Geology Padova*, *52*(1), 1–91.

Kuhlemann, J., & Kempf, O. (2002). Post-Eocene evolution of the North Alpine Foreland Basin and its response to Alpine tectonics. *Sedimentary Geology*, *152*(1–2), 45–78. https://doi.org/10.1016/s0037-0738(01)00285-8

Lallemand, S., Heuret, A., Faccenna, C., & Funiciello, F. (2008). Subduction dynamics as revealed by trench migration. *Tectonics*, *27*(3), 815. https://doi.org/10.1029/2007tc002212

Lanari, R., Reitano, R., Faccenna, C., Agostinetti, N. P., & Ballato, P. (2023). Surface and crustal response to deep subduction dynamics: Insights from the Apennines, Italy. *Tectonics*, *42*(3), e2022TC007461. https://doi.org/10.1029/2022tc007461

Larrey, M., Mouthereau, F., Do Couto, D., Masini, E., Jourdon, A., Calassou, S., & Miegebielle, V. (2022). Oblique rifting triggered by slab tearing and back-arc extension: The case of the Alboran rift in the eastern betics. *Solid Earth*, *500*, 1221–1244.

Lash, G. G. (1988). Along-strike variations in foreland basin evolution: Possible evidence for continental collision along an irregular margin. *Basin Research*, *1*(2), 71–83. https://doi.org/10.1111/j.1365-2117.1988.tb00006.x

Le Breton, E., Brune, S., Ustaszewski, K., Zahirovic, S., Seton, M., & Müller, R. D. (2021). Kinematics and extent of the Piemont–Liguria Basin–implications for subduction processes in the Alps. *Solid Earth*, *12*(4), 885–913. https://doi.org/10.5194/se-12-885-2021

Lemcke, K. (1988). Das bayerische Alpenvorland vor der Eiszeit.

Ma, L., Wang, B.-D., Jiang, Z.-Q., Wang, Q., Li, Z.-X., Wyman, D. A., et al. (2014). Petrogenesis of the Early Eocene adakitic rocks in the Napuri area, southern Lhasa: Partial melting of thickened lower crust during slab break-off and implications for crustal thickening in southern Tibet. *Lithos*, *196*, 321–338. https://doi.org/10.1016/j.lithos.2014.02.011

Margirier, A., Braun, J., Robert, X., & Audin, L. (2018). Role of erosion and isostasy in the Cordillera Blanca uplift: Insights from landscape evolution modeling (northern Peru, Andes). *Tectonophysics*, *728*, 119–129. https://doi.org/10.1016/j.tecto.2018.02.009

Marín-Lechado, C., Pedrera, A., Peláez, J. A., Ruiz-Constán, A., González-Ramón, A., & Henares, J. (2017). Deformation style and controlling geodynamic processes at the eastern Guadalquivir foreland basin (Southern Spain). *Tectonics*, *36*(6), 1072–1089. https://doi.org/10.1002/2017tc004556

Marzec, P., Sechman, H., Kasperska, M., Cichostępski, K., Guzy, P., Pietsch, K., & Porębski, S. J. (2018). Interpretation of a gas chimney in the Polish Carpathian Foredeep based on integrated seismic and geochemical data. *Basin Research*, *30*(S1), 210–227. https://doi.org/10.1111/bre.12216

Meulenkamp, J., Kováč, M., & Cicha, I. (1996). On late Oligocene to Pliocene depocentre migrations and the evolution of the carpathian-pannonian system. *Tectonophysics*, *266*(1–4), 301–317. https://doi.org/10.1016/s0040-1951(96)00195-3

Montgomery, D. R., & Brandon, M. T. (2002). Topographic controls on erosion rates in tectonically active mountain ranges. *Earth and Planetary Science Letters*, *201*(3–4), 481–489. https://doi.org/10.1016/s0012-821x(02)00725-2

Nagel, S., Granjeon, D., Willett, S., Lin, A. T.-S., & Castelltort, S. (2018). Stratigraphic modeling of the Western Taiwan foreland basin: Sediment flux from a growing mountain range and tectonic implications. *Marine and Petroleum Geology*, *96*, 331–347. https://doi.org/10.1016/j.marpetgeo.2018.05.034

Naylor, M., & Sinclair, H. (2008). Pro-vs. retro-foreland basins. *Basin Research*, *20*(3), 285–303. https://doi.org/10.1111/j.1365-2117.2008.00366.x

Okosun, E. A., & Osterloff, P. (2014). Ostracod, diatom and radiolarian biostratigraphy of the Niger Delta, Nigeria. *Earth Science Research*, *3*(1), 72–93. https://doi.org/10.5539/esr.v3n1p72

Ortner, H., Aichholzer, S., Zerlauth, M., Pilser, R., & Fügenschuh, B. (2015). Geometry, amount, and sequence of thrusting in the Subalpine Molasse of western Austria and southern Germany, European Alps. *Tectonics*, *34*(1), 1–30. https://doi.org/10.1002/2014tc003550

Ouchi, S. (2011). Effects of uplift on the development of experimental erosion landform generated by artificial rainfall. *Geomorphology*, *127*(1–2), 88–98. https://doi.org/10.1016/j.geomorph.2010.12.009

Parra, M., Mora, A., Jaramillo, C., Torres, V., Zeilinger, G., & Strecker, M. R. (2010). Tectonic controls on Cenozoic foreland basin development in the north-eastern Andes, Colombia. *Basin Research*, *22*(6), 874–903. https://doi.org/10.1111/j.1365-2117.2009.00459.x

Paxman, G., Watts, A., Ferraccioli, F., Jordan, T., Bell, R., Jamieson, S., & Finn, C. (2016). Erosion-driven uplift in the Gamburtsev Subglacial Mountains of East Antarctica. *Earth and Planetary Science Letters*, *452*, 1–14. https://doi.org/10.1016/j.epsl.2016.07.040

Piccolo, A., Kaus, B. J., White, R. W., Palin, R. M., & Reuber, G. S. (2022). Plume—Lid interactions during the Archean and implications for the generation of early continental terranes. *Gondwana Research*, *88*, 150–168. https://doi.org/10.1016/j.gr.2020.06.024

Poirier, J.-P., & Liebermann, R. (1984). On the activation volume for creep and its variation with depth in the Earth's lower mantle. *Physics of the Earth and Planetary Interiors*, *35*(4), 283–293. https://doi.org/10.1016/0031-9201(84)90022-0

Rögl, F., Hochuli, P., & Muller, C. (1979). Oligocene–early Miocene stratigraphic correlations in the Molasse Basin of Austria. Annales Geologiques des Pays Helleniques. *Tome Hors Series*, *30*, 1045–1050.

Royden, L., & Faccenna, C. (2018). Subduction orogeny and the Late Cenozoic evolution of the Mediterranean Arcs. *Annual Review of Earth and Planetary Sciences*, *46*(1), 261–289. https://doi.org/10.1146/annurev-earth-060115-012419

Schlunegger, F., & Castelltort, S. (2016). Immediate and delayed signal of slab breakoff in Oligo/Miocene Molasse deposits from the European Alps. *Scientific Reports*, *6*(1), 1–11. https://doi.org/10.1038/srep31010

Schlunegger, F., & Kissling, E. (2022). Slab load controls beneath the Alps on the source-to-sink sedimentary pathways in the Molasse basin. *Geosciences*, *12*(6), 226. https://doi.org/10.3390/geosciences12060226

Schmalholz, S. M. (2011). A simple analytical solution for slab detachment. *Earth and Planetary Science Letters*, *304*(1–2), 45–54. https://doi.org/10.1016/j.epsl.2011.01.011

Schmid, S., Fügenschuh, B., Kissling, E., & Schuster, R. (2004). *TRANSMED transects IV, V and VI: Three lithospheric transects across the Alps and their forelands. The TRANSMED Atlas: The Mediterranean Region from Crust to Mantle*. Springer Verlag.

Sinclair, H. (1997). Flysch to molasse transition in peripheral foreland basins: The role of the passive margin versus slab breakoff. *Geology*, *25*(12), 1123–1126. https://doi.org/10.1130/0091-7613(1997)025<1123:ftmtip>2.3.co;2

Sinclair, H., & Allen, P. (1992). Vertical versus horizontal motions in the Alpine orogenic wedge: Stratigraphic response in the foreland basin. *Basin Research*, *4*(3-4), 215–232. https://doi.org/10.1111/j.1365-2117.1992.tb00046.x

Sinclair, H., Coakley, B., Allen, P., & Watts, A. (1991). Simulation of foreland basin stratigraphy using a diffusion model of mountain belt uplift and erosion: An example from the central Alps, Switzerland. *Tectonics*, *10*(3), 599–620. https://doi.org/10.1029/90tc02507

Sinclair, H., & Naylor, M. (2012). Foreland basin subsidence driven by topographic growth versus plate subduction. *Bulletin*, *124*(3–4), 368–379. https://doi.org/10.1130/b30383.1

Spakman, W., & Wortel, R. (2004). A tomographic view on western Mediterranean geodynamics, the TRANSMED Atlas. In *The Mediterranean region from crust to mantle: Geological and geophysical framework of the Mediterranean and the surrounding areas* (pp. 31–52). Springer.

Spang, A., Burton, M., Kaus, B. J., & Sigmundsson, F. (2022). Quantification of volcano deformation caused by volatile accumulation and release. *Geophysical Research Letters*, *49*(10), e2021GL097502. https://doi.org/10.1029/2021gl097502

Sperner, B., Lorenz, F., Bonjer, K., Hettel, S., Müller, B., & Wenzel, F. (2001). Slab break-off–abrupt cut or gradual detachment? New insights from the Vrancea Region (SE Carpathians, Romania). *Terra Nova*, *13*(3), 172–179. https://doi.org/10.1046/j.1365-3121.2001.00335.x

Stefanick, M., & Jurdy, D. M. (1992). Stress observations and driving force models for the South American plate. *Journal of Geophysical Research*, *97*(B8), 11905–11913. https://doi.org/10.1029/91jb01798

Tetzlaff, D. M., & Harbaugh, J. W. (1989). *Simulating clastic sedimentation* (Vol. 1110). Springer.

Turcotte, D. L., & Schubert, G. (2002). *Geodynamics*. Cambridge University Press.

Van der Meulen, M., Meulenkamp, J., & Wortel, M. (1998). Lateral shifts of Apenninic foredeep depocentres reflecting detachment of subducted lithosphere. *Earth and Planetary Science Letters*, *154*(1–4), 203–219. https://doi.org/10.1016/s0012-821x(97)00166-0

van Hunen, J., & Allen, M. B. (2011). Continental collision and slab break-off: A comparison of 3-D numerical models with observations. *Earth and Planetary Science Letters*, *302*(1–2), 27–37. https://doi.org/10.1016/j.epsl.2010.11.035

Wilmsen, M., Fürsich, F. T., Seyed-Emami, K., Majidifard, M. R., & Taheri, J. (2009). The Cimmerian Orogeny in northern Iran: Tectono-stratigraphic evidence from the foreland. *Terra Nova*, *21*(3), 211–218. https://doi.org/10.1111/j.1365-3121.2009.00876.x

Wortel, M., & Spakman, W. (2000). Subduction and slab detachment in the Mediterranean-Carpathian region. *Science*, *290*(5498), 1910–1917. https://doi.org/10.1126/science.290.5498.1910

Zhu, D., Wang, Q., & Zhao, Z. (2017). Constraining quantitatively the timing and process of continent-continent collision using magmatic record: Method and examples. *Science China Earth Sciences*, *60*(6), 1040–1056. https://doi.org/10.1007/s11430-016-9041-x